Journal of Environmental Chemical Engineering 13 (2025) 115050

Contents lists available at ScienceDirect

Journal of Environmental Chemical Engineering

journal homepage: www.elsevier.com/locate/jece

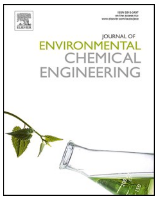

Production of chemicals *via* tandem conversion of bio-oil derived fractions

Evgeny Naranov[a,*], Alexey Sadovnikov[a], Olga Arapova[a], Alexander Guda[b], Konstantin Dementev[a], Ashot Arzumanyan[a,c], Gleb Kubrin[a,c,d], Dmitry Kholodkov[a,c], Alexander Zagrebaev[b], Kaige Wang[e], Zhongyang Luo[e], Anton Maximov[a]

[a] *Topchiev Institute of Petrochemical Synthesis, Russian Academy of Sciences, Leninsky prospekt, bld. 29, Moscow 119991, Russia*
[b] *The Smart Materials Research Institute, Southern Federal University, Sladkova 178/24, Rostov-on-Don 344090, Russia*
[c] *Nesmeyanov Institute of Organoelement Compounds, Russian Academy of Sciences, Vavilova Street, bld. 28, Moscow 119334, Russia*
[d] *D.I. Mendeleev University of Chemical Technology of Russia, Miusskaya sq., 9, Moscow 125047, Russia*
[e] *State Key Laboratory of Clean Energy Utilization, Zhejiang University, Hangzhou 310027, PR China*

ARTICLE INFO

Keywords:
Bio-oil
Guaiacol
Hydrodeoxygenation
Zeolites
Hydrosililation
in situ XANES

ABSTRACT

Studying chemical production from biomass is essential for developing sustainable and eco-friendly alternatives to fossil-derived chemicals, reducing greenhouse gas emissions, and promoting a circular bioeconomy. In this study a new biomass upgrading route was proposed including extraction of phenolic fraction followed by catalytic hydroconversion and then dehydration to olefins. The conversion of bio-oil fraction into olefins was developed using a continuous-flow setup with two reactors for tandem hydrogenation – dehydration process (225 °C in the 1st reactor with 2 % Ru over titanosilicalite-1 (TS-1) catalyst, 160 °C in the 2nd reactor with BEA catalyst, 5 MPa H_2, LHSV 1.5 h^{-1}). The optimized mild conditions were determined for each stage of the catalytic conversion process, which allowed us to obtain cyclohexene from bio-oil-derived compounds with a selectivity of up to 70 %. The olefin fraction was further transformed to silicon-organic chemicals *via* hydrosilylation on Pt catalyst. Using *in situ* DRIFT technique and *in situ* X-ray absorption spectroscopy (XAS) we determined the mechanism of selective hydrodeoxygenation and evolution of Ru species.

1. Introduction

The global economy has historically relied on fossil resources, with coal, oil, and natural gas accounting for over two-thirds of global energy production and fulfilling the entirety of humanity's demand for hydrocarbons as critical chemical feedstocks [1–4]. However, discoveries of large light oil reserves have become less frequent, and existing fields are steadily depleting [5,6]. In addition to resource depletion, the extensive use of fossil fuels contributes to significant anthropogenic carbon dioxide (CO_2) emissions [7–9]. This contributes to approximately 1.8 % of the total atmospheric CO_2. Since the pre-industrial era, atmospheric CO_2 concentrations have risen from 277 ppm (in 1750) to 395 ppm (in 2013), with the majority of this increase attributed to industrial activities [10–13]. Renewable resources, such as plant biomass, present the most viable alternative to fossil resources [14–17]. Biomass contains carbon, hydrogen, and oxygen, and thus has the potential to be utilized both for energy generation and the production of fuels and chemicals [1,18]. From a technological and economic perspective, the most promising approach to processing lignocellulosic biomass involves two stages: the thermochemical conversion of biomass (via liquefaction, gasification, or pyrolysis) to produce intermediate products (bio-oil), followed by their conversion into fuels or petrochemical products [1,2]. Among these methods, gasification and pyrolysis are the most developed and industrially applied [19–23]. However, integrating bio-oil into conventional petroleum refining processes, such as hydrotreating, hydrocracking, or catalytic cracking, presents challenges due to its immiscibility with hydrocarbon feedstocks, low thermal stability, and high coke formation [2,21,24]. Biomass generally contains a significant amount of water, reaching up to 50 wt%, resulting in the formation of an aqueous bio-oil solution during fast pyrolysis [25–27]. Therefore, bio-oil fractionation is essential for separating its complex mixture of oxygenated compounds into distinct fractions, facilitating their purification and targeted application in fuels, chemicals, and materials [28,29]. Upgrading these fractions through processes such as hydrodeoxygenation, catalytic cracking, or esterification improves their stability, energy content, and compatibility with existing fuel infrastructure [29]. The separation of

---

* Corresponding author.
E-mail address: naranov@ips.ac.ru (E. Naranov).

https://doi.org/10.1016/j.jece.2024.115050
Received 5 October 2024; Received in revised form 30 November 2024; Accepted 5 December 2024

bio-oil is considered an essential step prior to its upgrading. Kiss et al. have highlighted the critical role of separation technologies in establishing biorefineries as a viable and successful concept [30]. Hydrogenation and hydrocracking of bio-oil have emerged as the most promising methods for upgrading liquefied biomass [2,24,31]. These processes are typically carried out at temperatures ranging from 200 to 400 °C, under high hydrogen pressures up to 30 MPa, in the presence of catalysts such as noble metals or transition metal sulfides (e.g., cobalt, nickel, and molybdenum) [18,32–37]. The upgraded bio-oil can contain up to 70 % hydrocarbons, with its oxygen content reduced to 5–10 %, making it a potential substitute for conventional hydrocarbon-based products [2,38,39]. Numerous studies have reported on the hydroprocesses of bio-oils using various heterogeneous and homogeneous catalysts [24,34–36,40–42]. There are reports on highly active heterogeneous catalysts composed of different transition and precious metals [1,2,34,43]. Among these catalysts, ruthenium is noted for its oxophilicity, high activity in aqueous-phase HDO, and relative cost-effectiveness [37,44–47]. The activity of Ru in water can be attributed to the interaction between adsorbed water molecules and the substrate at the active sites through hydrogen bonding [31,43,45,47–50]. In our previous studies, we have revealed the significance of ruthenium species in the oxidized state during bio-oil substances hydroconversion [31,37]. It was established that the hydrous ruthenium oxide state was more active compared to pure metallic state due to the substrates adsorption preferences.

Here we present a catalytic scheme of highly valued silicon-organic chemicals production using bio-oil as a feedstock (Scheme 1). Hydrosilylation of unsaturated hydrocarbons is a key atom-economical method for forming Si–C bonds [51–54]. For this purpose, a selective extraction of the phenolic fraction of bio-oil (C6-C9) was performed, which was then converted into olefins through a two-stage hydrogenation – dehydration catalytic process. The hydrosilylation of obtained olefin fraction allowed the production of organosilicon compounds with quantitative yield.

2. Experimental section

2.1. Catalysts synthesis

The TS-1 catalytic material was synthesized using modified protocol developed by Liu and co-authors [55]. In a typical of synthesis of TS-1, 9.3 g of TPAOH (Sigma-Aldrich, aqueous solution 25 wt%) mixed with 2.3 g deionised water was added dropwise into 7.5 g TEOS (Sigma-Aldrich) under stirring, then 0.32 g tetra-*n*-butyl orthotitanate (Sigma-Aldrich) dissolved in 1.2 g isopropyl alcohol (> 99,9 %, Reachem) was slowly added to the above mixture under vigorous stirring. After keep stirring for another 20 min, the mixture was kept at 70 °C for about 2 h to remove isopropyl alcohol, and then the precursor solution were obtained. The precursor was transferred to a Teflon-lined steel autoclave equipped with magnetic stirrer and placed into special heating furnace. The crystallization was carried out at a stirring rate of 500 rpm in order to produce uniform particles at 160 °C for 72 h. After crystallization, the solid product obtained by centrifugation was washed with ethanol and distilled water, dried at 80 °C overnight, and then calcined at 550 °C for 6 h.

The loading of the metal (1 – 5 wt% Ru) onto TS-1 was done by incipient wetness impregnation using the solution of ruthenium chloride ($RuCl_3 \cdot H_2O$, «Aurat», ω(Ru) ≥ 46.0 wt%) as the metal precursor. In a typical synthesis of Ru-containing catalysts, the calculated amount of ruthenium chloride was dissolved in methanol. Then, a porous material (calcined at 550 °C) was added to $RuCl_3$ solution under stirring and kept at room temperature overnight. The sample was dried at 90 °C for 12 h and then at 120 °C for 6 h followed by calcination at 500 °C for 5 h. The catalysts were denoted as *n*Ru/TS-1, where *n* was the metal content – 1, 2 or 5 wt%.

2.2. Catalytic experiments

Conversion of oxygen-containing substances was conducted in two regimes: closed mixing reactor (autoclave) and a continuous-flow setup with two reactors. Hydrogenation in a mixing reactor was conducted in a steel autoclave equipped with a magnetic stirrer and a pressure gauge [31,56]. The autoclave was charged with 0.050 g of catalyst, 1.00 g of guaiacol and 3,00 g of *n*-heptane (inner volume of autoclave - 40 mL). The bio-oil was purchased from BTG (Netherlands), the detailed composition of bio-oil was showed in [57]. The autoclave was filled with hydrogen to a pressure of 5 MPa. The reaction was run at 200–300 °C with a stirrer speed of 700 rpm. After the reaction, the autoclave was cooled to room temperature and the pressure was decreased to atmospheric pressure.

The catalytic conversion of guaiacol and bio-oil fraction into cyclohexene was performed in a continuous-flow setup with two reactors (Fig. 1). The both reactors were stainless steel with an internal diameter of 11.6 mm and a length of 250 mm. The catalysts powders were pressed in tablets and then crushed. The fraction of 0.6 – 1.0 mm was used for Ru/TS-1 and BEA catalysts (Zeolyst, CP814E). The loaded catalysts volume of Ru/TS-1 and BEA were 10 mL (6.7 and 3.6 g respectively). The quartz fraction of 1.0–1.6 mm was placed under and upper the catalyst layer. The substrate in *n*-heptane solution was pumped from vessel by a syringe pump (500D, Teledyne ISCO) to the 1st reactor with Ru/TS-1 catalysts and further into the 2nd reactor with BEA catalyst. The pressure in the system was regulated by the pressure valve (Equilibar). The separation of liquid products from gas flow took place in the separator. Separator was operated under atmospheric pressure and it was cooled through the jacket with cold water ~ 8 °C. The measurement of gas outflow quantity was carried out using a gas clock (volumetric diaphragm-type gas meter). Hydrogen was supplied from a gas cylinder

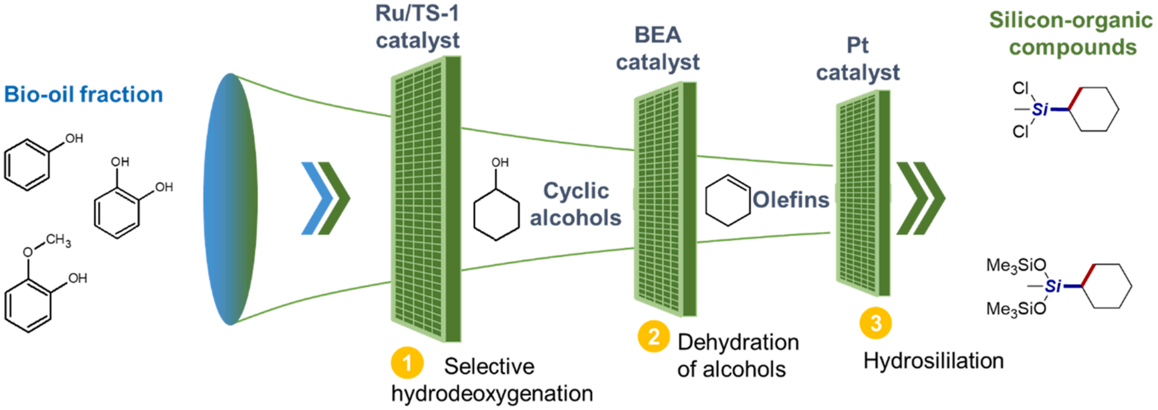

Scheme 1. A catalytic scheme of silicon-organic compounds production using bio-oil fraction as a feedstock.

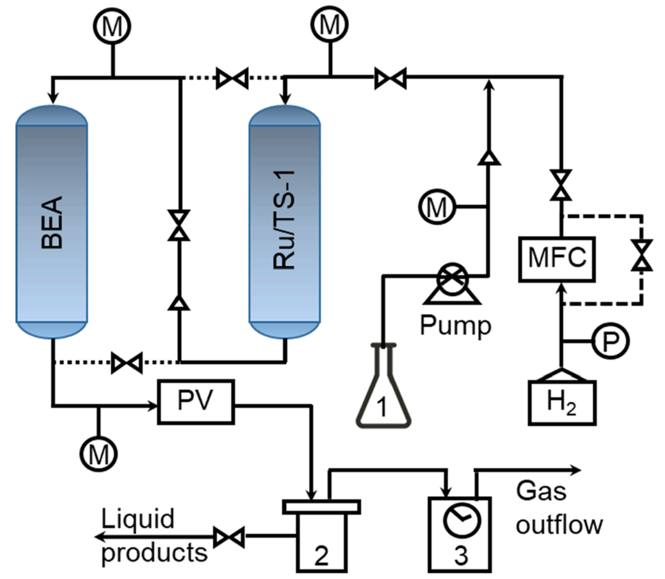

Fig. 1. Schematic diagram of the double reactor experimental setup (1 – Substrate vessel, 2 – Separator, 3 – Gaseous clock, M – manometer, P – gas reducer, MFC – Mass flow controller, PV – Pressure valve, Δ – filter, ⋈ – valve, the dotted line indicates the bypass line).

through gas reducer P. The hydrogen inflow was measured and controlled by a mass flow controller (Bronkhorst).

The separate experiments of guaiacol hydrogenation and cyclohexanol dehydration were conducted *via* bypassing the 2nd reactor with BEA and the 1st reactor with Ru/TS-1 respectively by closing the corresponding valves. Therefore, contact between the cyclohexanol solution and the Ru/TS-1 catalyst was avoided, as well as contact between the guaiacol solution and the BEA catalyst. The substrate for dehydration on the BEA catalyst contained 10 % cyclohexanol in *n*-heptane (separate process without hydrogenation), while the substrate for hydrogenation on the Ru/TS-1 catalyst contained 10 % guaiacol in n-heptane (separate process without dehydration). For the tandem hydrogenation-dehydration process, the substrate was 10 wt% guaiacol or 5 wt% bio-oil fraction in *n*-heptane.

The qualitative composition of the liquid products was determined by gas chromatography - mass spectrometry (GC-MS) using a Finnigan MAT 95 XL instrument equipped with a Varian VF-5MS capillary column and helium as a carrier gas (1.5 cm^3/min). Temperature programming was conducted as follows: holding at 34 °C for 5 min, heating to 290 °C (10 °C/min), holding for 10 min. The concentrations of the products were calculated by the ratio between the corresponding peak area and the sum of the area of the peaks considering the response factors of pure substances. The results were processed using the Xcalibur software package. The products were identified by matching their mass spectra against the dedicated mass spectra library of the software.

The C, H, N and S content of the samples was studied by chromatography after combustion in a dynamic flash on a THERMO FLASH 2000 elemental CHNS analyzer. Before analysis, the samples were homogenized by shaking for several minutes. The oxygen content was calculated by difference.

The water content in the bio-oil samples was measured using the Karl-Fischer method on an Expert-007M titrator using volumetric titration.

Structural features and changes of acid sites of Ru- catalysts and intermediates formed during hydrogenation of guaiacol were studied using *in situ* high-temperature diffuse reflectance infrared Fourier transform (DRIFT) spectroscopy, which made it possible to measure the infrared (IR) spectra of zeolite catalysts at 200 – 250 °C in a dry hydrogen flow. The sample was placed in a PIKE Diffuse IR high-temperature cell coupled with a Bruker VERTEX-70 FTIR spectrometer. Spectra were taken in a continuous mode (194 scans/spectrum) with a resolution of 2 cm^{-1} in the range of 4000–600 cm^{-1}. The Y axis in the spectra corresponds to the optical density ($D = \log(I_0/I)$). At first, the catalysts were heated up to 450 °C in an Ar atmosphere, then the temperature was decreased to 200, 225 or 250 °C when the substrate and hydrogen flow was turned on. The saturated guaiacol vapors were introduced *via* a dry hydrogen flow-driven bubbler system. An outlet positioned downstream of the high-temperature cell facilitated the release of reaction products. The, guaiacol was introduced to the catalytic system by hydrogen flow at a rate of 0.7 L/h, ensuring that guaiacol remained in the vapor phase under the experimental conditions, preventing condensation and the formation of liquid guaiacol within the system. After that, the spectra were recorded for one hour.

Hydrosililation of bio-oil fraction after tandem process was conducted using following protocol: in a Schott tube, under argon atmosphere, cyclohexene fraction (> 2.5 wt% in *n*-heptane, 1 eq, 0.09 mmol, 284 mg) and hydrosilane (3 eq, 0.27 mmol, 60 mg of bis(trimethylsiloxy)methylsilane or 31 mg di(chloro)methylsilane) were mixed, then [Pt] (Karstedt's catalyst [58], 2 wt% Pt solution in xylene, used as purchased, 0.1 mol%, 0.001 eq, 1 μL) was added to a stirring mixture of reagents. The resulting mixture was stirred at 60 °C for 24 h. Reaction mixture was analyzed using GLC and ^{1}H, ^{13}C and ^{29}Si NMR. Yield was determined by ^{1}H NMR data.

2.2.1. *Cyclohexyl-methyl-bis(trimethylsiloxy)silane*

^{1}H NMR (400 MHz, $CDCl_3$): δ = 1.67 (m, 4 H), 1.18 (m, 4 H), 1.08 (m, 2 H), 0.47 (m, 1 H), 0.07 (s, 18 H), 0.06 (s, 3 H). ^{13}C {^{1}H} NMR (100 MHz, $CDCl_3$): δ = 33.2, 27.6, 27.0, 1.9, –2.8. ^{29}Si NMR (80 MHz, $CDCl_3$): δ = 7.2, –23.8.

2.2.2. *Dichloro-cyclohexyl-methylsilane*

^{1}H NMR (400 MHz, $CDCl_3$): δ = 2.09 (m, 2 H), 2.01 (m, 2 H), 1.95 (m, 1 H), 1.47 (m, 5 H), 1.30 (m, 1 H), 0.92 (s, 3 H). ^{13}C {^{1}H} NMR (100 MHz, $CDCl_3$): δ = 30.76, 27.23, 26.42, 25.82, 3.19. ^{29}Si NMR (80 MHz, $CDCl_3$): δ = 32.5.

2.3. *Characterization*

The textural characteristics of the samples were determined by low-temperature nitrogen adsorption (77 K) using a Micromeritics ASAP 2020 instrument. Prior to analysis, the samples were degassed at 350 °C for 6 h. The specific surface area was calculated by Brunauer-Emmett-Teller (BET) theory at a relative partial pressure of $P/P_0 = 0.2$; the pore size distribution was calculated according to the Barrett–Joyner–Halenda (BJH) model using adsorption data following the approach proposed by Ryoo and co-workers [59].

The composition of the samples was analyzed by atomic absorption spectrometry using a PerkinElmer Analyst instrument.

X-ray powder diffraction analysis was carried out using a Rigaku D/MAX 2500 diffractometer (CuK_α radiation) in the 2Θ range of 1–50°, with a goniometer rotation speed of 1°min^{-1}. The X-ray phase analysis of the samples after catalysis was carried out from the suspension without preliminary drying.

The XPS measurements were performed using a «PREVAC EA15 » electron spectrometer. In the current work, AlKα (hν = 1486.6 eV, 150 W) were used as a primary radiation source. The pressure in analytical chamber did not exceed 5×10^{-9} mbar during spectra acquisition. The binding energy (BE) scale was pre-calibrated using the positions of Ag$3d_{5/2}$ (368.3 eV) and Au$4f_{7/2}$ (84.0 eV) from silver and gold foils, respectively. The powdered catalyst samples were supported onto double-sided conducting scotch tape. The spent 5Ru/TS-1 catalyst suspended in the liquid products was transferred to the holder of the XPS system in order exclude the air exposure. To take into account the effect of surface charging, the C1s at (E_b = 284.8 eV) from the carbon contamination was used as an internal standard.

Temperature-programmed reduction with hydrogen (TPR-H_2) was performed using AutoChem 2950HP instrument (Micromeritics Instrument Corp., Norcross, GA, USA). In a typical procedure, a sample was purged with Ar flow at 400 °C for 1 h, then cooled down to 50 °C. The reduction was performed under the 30 mL/min flow of 8 vol% H_2–92 vol% Ar mixture in the range of 50 °C–400 °C with a ramp of 10 °C/min.

Raman spectra of catalysts were acquired in the range from 3700 to 100 cm^{-1} by using a Senterra II confocal Raman microscope (Bruker) using a 532 nm laser (0.25 mW) for the TS-1 sample, and with the 50 × ocular. Acquisition time was 9 s, 25 scans were recorded and averaged for each sample.

Attenuated total reflection infrared (ATR-IR) spectra of all the samples were recorded in the range of 2000–400 cm^{-1} on a Bruker ALPHA instrument equipped with a diamond tool.

TGA was performed on Mettler TA 4000 system. The heating and cooling of samples was performed at a rate of 10 °C/min under air flow of (70 mL/min) in the range of −20 °C to 800 °C.

Temperature-programmed desorption of ammonia (NH_3-TPD) was performed using USGA-101 instrument. The samples were pretreated at 500 °C for 1 h in a helium flow, and then NH_3 adsorption was carried out at 110 °C temperature in 10 vol% NH_3 in helium with a flow of 30 cm^3/min. Subsequently, the physically adsorbed NH_3 on the TS-1 sample was purged by the helium flow at 110 °C for 1 h. The signal of NH_3 desorption was recorded in the temperature range up to 500 °C with a heating rate of 10 °C/min.

Fourier transform infrared (FTIR) spectra were recorded on The Nicolet iS10 spectrometer. Prior to the measurements, the catalysts were pressed into self-supporting disks and activated in the IR cell attached to a vacuum line at 673 K for 2 h. Adsorption of pyridine was performed at 423 K for 20 min. Excess probe molecules were further evacuated at 423 K for 20 min. The numbers of Brønsted and Lewis acid sites were determined from the intensities of the bands at ca. 1545 and 1455 cm^{-1} of adsorbed pyridine, respectively, using the molar extinction coefficients given by Tamura et al. [60].

Scanning electron microscopy (SEM) images and energy-dispersive X-ray (EDX) spectra were recorded using an NVision 40 microscope (Carl Zeiss) equipped with the X-Max 80 EDX detector (Oxford Instruments).

For transmission electron microscopy (TEM) FEI's Tecnai Osiris TEM with an accelerating voltage of 200 keV was used. Scanning electron microscopy (SEM) images and energy-dispersive X-ray (EDX) spectra were recorded using an NVision 40 microscope (Carl Zeiss) equipped with the X-Max 80 EDX detector (Oxford Instruments).

2.4. *In situ XANES studies*

Ruthenium local coordination and oxidation state were monitored with X-ray absorption spectroscopy (XAS) in the near-edge energy region (XANES) and extended energy region (EXAFS). *In situ* Ru K-edge XAS were acquired at the STM beamline of the Kurchatov synchrotron radiation facility (Moscow, Russia). The storage ring operated at 2.5 GeV electron beam energy with a current of 80–100 mA. All spectra were collected in the transmission mode using a Si(220) channel-cut monochromator. The incident beam intensity and the intensities after the autoclave and reference pellet were monitored using three ionization chambers. A special home-made autoclave-type *in situ* cell was designed to collect the data in transmission mode [56]. The body of autoclave was equipped with two coaxial holes for the X-ray beam. After pressurizing with 5 MPa of hydrogen the autoclave was placed inside a furnace with coaxial holes of a bigger diameter and intense magnetic stirring was started. The frequency of stirring was adjusted compromise between sedimentation and turbulence affecting quality of XAS data from a small volume of reaction mixture.

Post-processing of the data (energy alignment, averaging, background subtraction and normalization) was performed in the Athena program from the Demeter package [61]. Further analysis in Artemis program included calculation of theoretical amplitudes and phases by the FEFF6 code and fitting in the R-space of the Fourier-transformed data k^2- weighted $\chi(k)$ applying Δk Hanning window from 2.0 to 10.0 Å^{-1} with the width of the window slope dk = 1 Å^{-1}. The range in R-space for fit was 1.1 … 2.0 Å for the sample at room temperature to account for the Ru-O scattering in the first coordination sphere and 1.1 … 2.5 Å for sample at 200 °C to account additionally for the Ru-Ru scattering from metal phase. For each sample several fits were performed starting from different initial conditions. We ensured that number of parameters for each fit didn't exceed the number of independent points N_{ind}, defined as $N_{ind} = (2\Delta r\Delta k/\pi) + 1$, where Δk – is the region of EXAFS spectrum in k-space used for the Fourier analysis, Δr – is the region in R-space for the Fourier filtration.

3. Results and discussion

3.1. *The structure analysis*

The physical-chemical characterization of the synthesized TS-1, assessed through N_2 isotherms, SEM and TEM micrographs, and XRD patterns, provides detailed insights into its structural and compositional properties, affirming its high crystallinity, uniform microporosity, and the successful incorporation of titanium into the MFI zeolite framework. The nitrogen adsorption-desorption isotherms of TS-1 exhibit the Ist type isotherm (according to the IUPAC classification), which is indicative of microporous materials, characterized by a steep uptake at low relative pressures ($P/P_o < 0.1$) that corresponds to micropore filling. The hysteresis loop at $P/P_0 = 0.9$ is attributed to the condensation inside the voids between the nanocrystals, corroborating the small size of the TS-1 material (Fig. 3) [62]. The BET surface area is 430 m^2/g, while the micropore volume, derived from the *t*-plot method, is 0.15 cm^3 /g. Textural characteristics have been calculated from N_2 isotherms and given in Table 1.

SEM analysis reveals the morphology and surface characteristics of TS-1 crystallites. The SEM micrographs depict well-defined crystallites with prismatic shapes, typical of MFI-type zeolites, and crystal sizes generally ranging from 100 to 150 nm (Fig. 2A, B). These images indicate a homogeneous distribution of particles with smooth surfaces, devoid of visible defects or impurities, which underscores the high purity and well-formed crystalline structure of the material. TEM analysis offers nanoscale insights (Fig. 2C), where it reveals the highly ordered nature of the MFI framework, with distinct lattice fringes corresponding to the zeolitic structure. EDX analysis confirms the introduction of titanium inside the MFI structure, indicating that titanium is well-dispersed and substitutionally incorporated into the zeolite framework (Fig. S2, Table S1).

X-ray diffraction (XRD) patterns of TS-1 are indicative of the MFI zeolite structure (Fig. 3B), displaying characteristic reflections at 2θ values of approximately 7.9°, 8.9°, 23.1°, and 23.9°, corresponding to the (011), (200), (051), and (303) planes, respectively [63]. These reflections confirm the high crystallinity of TS-1 and suggest that the incorporation of titanium into the framework does not alter the overall MFI structure. The XRD patterns showed no reflecions at 2θ 25.4° and 27.7° indicating the absence of anatase and rutile TiO_2 respectively

Table 1
Characteristic of supports and RuO_2 catalysts.

Sample	S_{BET}. m^2/g$^{(a)}$	Average particles size, nm$^{(b)}$	Ru content, wt%$^{(c)}$
TS−1	430	-	-
1Ru/TS−1	425	2.3	4.8
2Ru/TS−1	422	2.6	1.9
5Ru/TS−1	415	8.2	1.0

(a) BET specific surface area from adsorption isotherm in the relative pressure range 0.05–0.20, (b) by TEM analysis, (c) ICP/OES analysis.

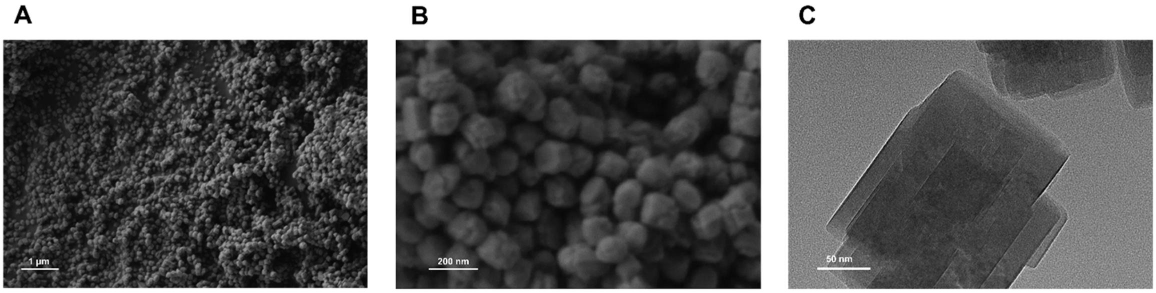

Fig. 2. SEM (A, B) and TEM (C) images of TS-1.

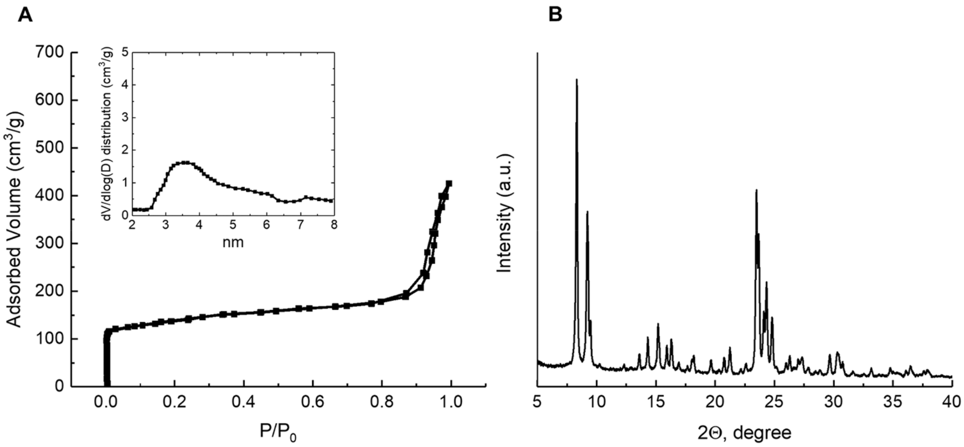

Fig. 3. (A) N_2 adsorption–desorption isotherm and the corresponding pore size distributions calculated by applying NL-DTF to the absorption branch, (B) XRD patterns of TS-1.

[64]. The absence of extraneous reflections indicates no detectable amorphous phases or impurities, reinforcing the material's high purity.

In the ATR-IR spectrum of TS-1, the presence of framework Ti^{4+} can be identified by specific vibrational bands (Fig. 4 A). A key feature indicative of Ti^{4+} incorporation into the zeolite framework is the presence of a band around 972 cm^{-1} . This band is attributed to the asymmetric stretching vibration of Si–O–Ti bonds, confirming that titanium is tetrahedrally coordinated within the silica framework [64]. The position and intensity of this band provide evidence that titanium atoms are substitutionally incorporated into the zeolite structure rather than existing as extraframework species. The absence of extraframework Ti species can be further confirmed by the lack of additional bands typically associated with non-framework titanium. Extraframework Ti species, such as TiO_2, would exhibit characteristic IR bands around 800 cm^{-1} (Ti–O stretching) and 470 cm^{-1} (Ti–O bending) [65].

Furthermore, the ATR-IR spectrum typically exhibits the characteristic bands of the MFI-type zeolite framework, such as the intense bands around 550 cm^{-1} , associated with the double five-ring units of the MFI structure, and the bands in the range of 1100–1225 cm^{-1} , corresponding to the asymmetric stretching vibrations of Si–O–Si linkages. The presence of these bands, along with the band at 972 cm^{-1} , reinforces the successful incorporation of Ti^{4+} into the zeolite framework while maintaining the integrity of the MFI structure [64].

In the Raman spectrum of TS-1 there are two intensive bands at 1125, 975 cm^{-1} and a complex absorption at 820 cm^{-1} (Fig. 4B). The bands at 1125 and 975 cm^{-1} have been associated with the symmetric stretching vibration and the asymmetric stretching of the framework TiO_4 respectively. The absence of any bands related to bulk TiO_2 phases indicates the high dispersion of titanium in the framework.

In the NH_3-TPD profiles, the peaks are typically divided into two distinct regions: below and above 400 °C, corresponding to low-temperature and high-temperature regions, respectively. The low-temperature peaks are associated with weak acid sites, while the high-temperature peaks are attributed to strong acid sites, including both Brønsted and Lewis types [66]. As shown in Fig. 4 C, the observed peaks appear exclusively in the low-temperature region, indicating the presence of only weak Lewis acid sites on the surface of TS-1 at a concentration of 90 μmole/g. The acidity determined by FTIR of adsorbed pyridine reveals a clear distinction between Brønsted and Lewis acid sites (Fig. 4D). The absorption band at 1446 cm^{-1} is attributed to pyridine coordination with Lewis acid sites, while the signal at 1490 cm^{-1} corresponds to an overlap of Brønsted and Lewis acid sites [67]. The near absence of the absorption band at 1545 cm^{-1} indicates the exclusive presence of Lewis acid sites, with no detectable Brønsted acid sites in the TS-1 sample.

3.2. Characterization of Ru containing catalysts

The synthesized TS-1 material was used to obtain Ru catalysts with the different content of ruthenium – 1, 2 and 5 wt% using incipient wetness impregnation. As shown in Fig. S3, a high dispersion of the Ru species was achieved in 1Ru/TS-1 and 2Ru/TS-1.The average Ru-particles size was 2.3 in the case of 1Ru/TS-1 and 2.6 nm in the case of 2Ru/TS-1. It should be noted that more than 80 % of Ru-particles are in the range from 0.5 to 3.5 nm. A narrow particle size distribution was obtained as a result of the uniform TS-1 structure and low metal content. On the other hand, the 5Ru/TS-1 sample contained sufficiently large nanoparticles with the average size of > 8 nm. This phenomenon can likely be attributed to the fact that, at this metal concentration and microporous support structure, particle agglomeration occurs. This is corroborated by the bimodal particle size distribution observed in 5Ru/TS-1, indicating the presence of smaller particles, similar to those in samples 1Ru/TS-1 and 2Ru/TS-1, as well as larger particles on the surface of the TS-1 nanocrystals.

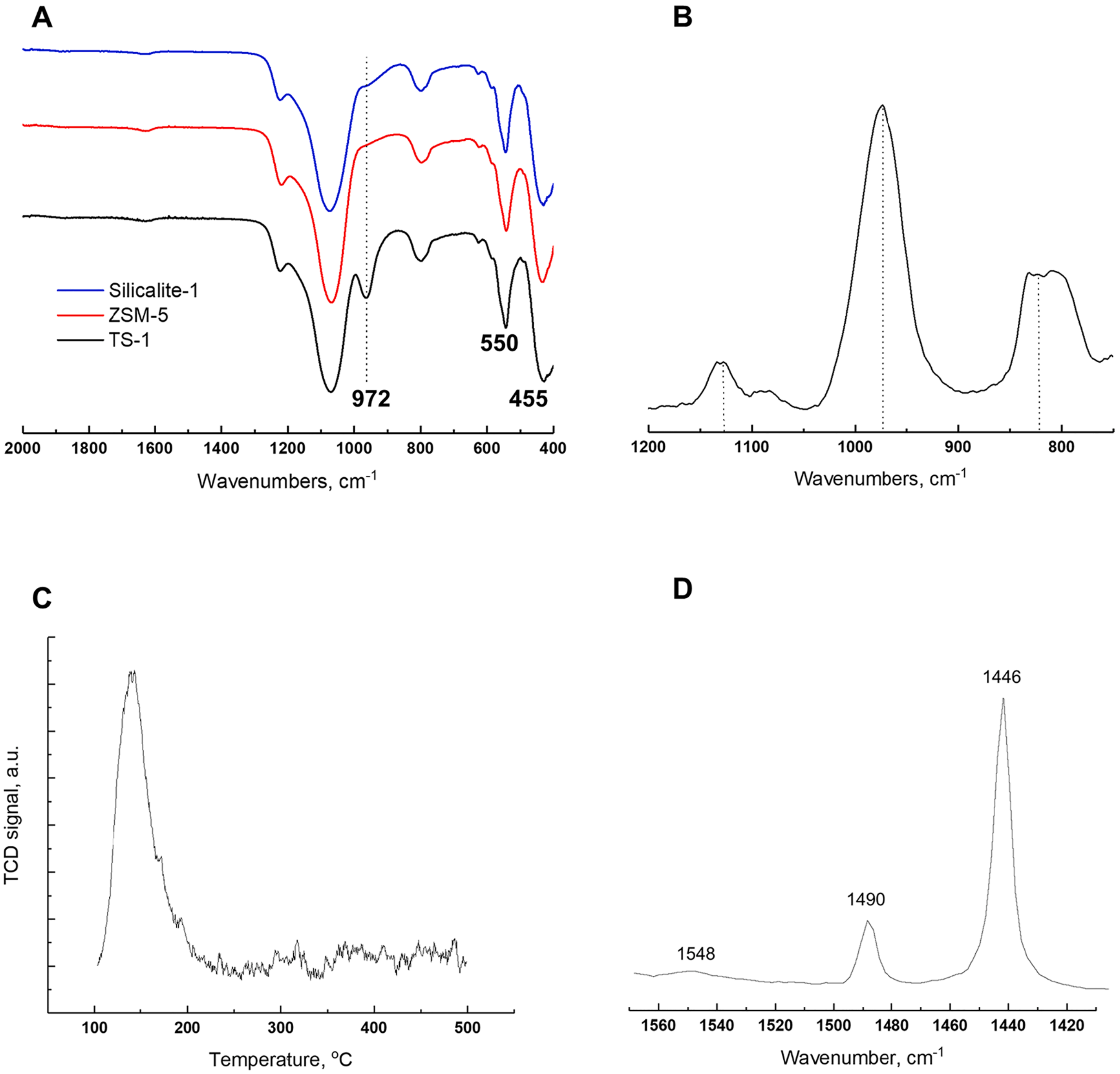

Fig. 4. (A) FT-IR spectra of TS-1, ZSM-5 and Silicalite-1, (B) Raman spectra of TS-1 sample, (C) NH_3 - TPD curves obtained on TS-1, (D) FTIR spectra of pyridine adsorbed over TS-1.

The phase composition data of the Ru-supported catalysts was done using XRD and XPS, and the results are showed in Fig. S4 and S5 respectively. Only with the ruthenium content of 5 wt% the reflections are intense enough to separate from those of TS-1. The reflexes at 2θ of 28°, 35° and 54° correspond to the (100), (002), and (101) planes, respectively, of RuO_2 phase (JCPDS # 65–2884). The crystallite sizes of RuO_2 nanoparticles determined from the Scherrer formula was about 24 nm. This overestimation of particle size is caused by the feature of

Table 2
Selectivity over different catalysts. Reaction conditions: 200 – 300 °C, 5 MPa H_2, catalysts mass 0.05 g.

	1Ru/TS-1			2Ru/TS-1			5Ru/TS-1		
0.5 h	**200 °C**	**250 °C**	**300 °C**	**200 °C**	**250 °C**	**300 °C**	**200 °C**	**250 °C**	**300 °C**
Conversion, %	70	75	76	74	77	90	75	81	90
2-methoxycyclohexanol	95	92	41	92	75	35	92	73	33
cyclohexanol	5	8	54	8	25	60	8	26	62
cyclohexane	0	0	5	0	0	5	0	1	5
1 h									
Conversion, %	81	95	100	88	100	100	90	100	100
2-methoxycyclohexanol	88	85	30	80	63	24	81	57	24
cyclohexanol	12	15	56	20	36	66	19	38	66
cyclohexane	0	0	14	0	1	10	0	5	10
3 h									
Conversion, %	100	100	100	100	100	100	100	100	100
2-methoxycyclohexanol	85	75	11	82	49	6	82	45	6
cyclohexanol	15	20	49	17	43	53	17	39	53
cyclohexane	0	5	40	1	8	41	1	16	41

smaller nanoparticles, due to their amorphous X-ray nature.

The catalytic hydrogenation of guaiacol was investigated using Ru catalysts supported on TS-1 with varying Ru contents of 1 %, 2 %, and 5 %. Reactions were conducted in an autoclave at 200–300 °C under 5 MPa H₂ pressure, with reaction times of 0.5–3 h. The catalyst mass was 50 mg, guaiacol was 1 g, and *n*-heptane served as the solvent (3 g). The experiments demonstrated that the Ru catalyst exhibited high activity with the selectivity towards hydrogenation products being strongly influenced by temperature (Table 2). In the catalytic series, guaiacol conversion exceeded 60 % within 1 h. At 250 °C, the conversion was moderate, yielding partially hydrogenated products, with high selectivity towards fully hydrogenated product – 2-methoxycyclohexanol. At 300 °C, a high level of hydrodeoxygenation was achieved within 1 h.

At 200 °C, at the beginning of reaction, the 1 % Ru catalyst exhibited moderate guaiacol conversion (70 %) with significant fully hydrogenated product. The 2 % Ru and 5 % Ru catalyst showed improved performance with 74–75 % conversion and higher selectivity towards cyclohexanol. At 250 °C, the 1 % Ru catalyst reached 75 % conversion, the 2 % Ru catalyst achieved 77 %, and the 5 % Ru catalyst approached 81 % conversion, all with high selectivity for fully hydrogenated products. Extending the reaction time to 3 h led to almost full conversion for all catalysts, with higher selectivity towards HDO products – cyclohexanol and cyclohexane. At 300 °C, all catalysts exhibited high guaiacol conversions within 0.5 h: 76 % for the 1 % Ru catalyst and 90 % for the 2 % and 5 % Ru catalysts. The selectivity for HDO products was lower for the 1 % Ru catalyst, with high content of fully hydrogenated products, while the 2 % and 5 % Ru catalysts maintained higher selectivity towards cyclohexanol and cyclohexane. The presence of Lewis acid sites in Ru-containing porous catalysts is crucial for the selective hydrogenation of guaiacol to cyclohexanol, as these sites promote partial hydrogenation while preserving hydroxyl groups (Table 2). This selective pathway prevents over-deoxygenation, allowing the conversion to cyclohexanol rather than cyclohexane. In contrast, catalysts with Brønsted acid sites favor complete deoxygenation, leading to the formation of cyclohexane [31,68]. Therefore, controlling the nature of acid sites is essential for achieving the desired selectivity in bio-oil upgrading processes aimed at producing oxygenated intermediates.

The reusability of the catalysts was assessed, with the 1 % and 2 % Ru catalysts demonstrating excellent stability over 3 reaction cycles, maintaining consistent activity and selectivity. The 5 % Ru catalyst showed a slight decline in performance after repeated cycles, likely due to the higher Ru content leading to more significant catalyst deactivation. The ICP-OES elemental analysis showed that the content of Ru in the case of 5Ru/TS-1 catalyst decreased to 4.2 %. For the 1 % and 2 % Ru catalysts the final content of Ru were 0.9 and 1.7 % respectively. In conclusion, the catalytic hydrogenation of guaiacol using Ru/TS-1 catalysts with varying Ru content revealed that higher Ru loadings (2 % and 5 %) significantly enhance catalytic activity and selectivity towards HDO products. The 2 % Ru catalyst emerged as the optimal choice, balancing high conversion rates, selectivity, and stability. The 5 % Ru catalyst provided similar performance but with marginally higher costs and less stability. The 1 % Ru catalyst, while effective, showed lower activity and stability, requiring longer reaction times and higher temperatures to achieve comparable results.

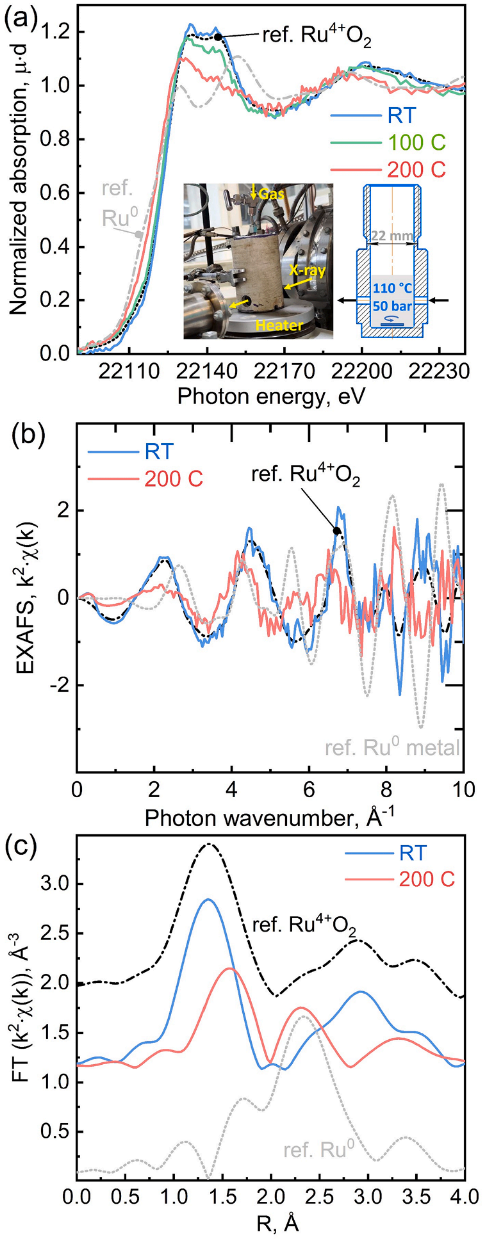

Fig. 5. Experimental Ru K-edge X-ray absorption spectra acquired in situ upon heating reaction mixture in H_2 atmosphere. (A) Normalized XANES spectra. Inset shows photo of experimental setup and scheme for the inner part of the autoclave. (B), (C) $k^2 \cdot \chi(k)$ and the amplitude of the Fourier transformed signal. Spectra of metal foil and RuO_2 are shown for comparison in each panel. Reaction conditions: 10 % of guaiacol in aqueous solution, 100 °C, 200 °C, 5 MPa H_2, 700 rpm.

3.3. *In situ evolution of Ru-species under high pressures and temperatures*

Ru *K*-edge XANES spectra of the 2Ru/TS-1 catalyst were collected using the high-pressure autoclave developed in our previous studies [31,56]. Fig. 5 shows experimental Ru K-edge XAS spectra collected *in situ* from the catalytic mixture at 25 °C, 100 °C, 200 °C. The measurements were performed from the sealed autoclave pressurized to 5 MPa of hydrogen at room temperature. The major changes in the spectra occurred rapidly after the temperature stabilized and we collected several spectra as the conditions inside the autoclave became stable. In a hydrocarbon solution, such as *n*-heptane, the reduction of the ruthenium oxide to the metallic state occurs quite quickly [37]. The XPS analysis of the 5 % Ru catalyst – 5Ru/TS-1 catalyst before and after hydrogenation process in *n*-heptane solution (200 °C, 5 MPa H_2, 1 h) revealed the full phase transition to Ru(0) (Fig. S5). In an aqueous solution, the reduction process slows down, allowing for a more precise detection of phase transformations. In our previous study, we demonstrated that even after 3 h of hydrogenation, the final state of the Ru-containing catalyst remained only partially metallic [31]. Therefore, for the *in situ* experiments water was used as a solvent.

In the XANES energy region (Fig. 5A) spectrum at room temperature coincides with the RuO_2 reference indicating presence of 6-coordinated Ru^{4+} ions in the catalyst with the oxygen ligands. At elevated temperatures, the shape of the spectrum and position of the absorption edge indicate simultaneous reduction and structural reorganization. The red curve measured at 200 °C is described by ~3 eV lower position of the absorption edge. The intensity of the white line became smaller indicating distortion of geometry from octahedral to the one with smaller coordination number. According to the semi-empirical Natoli's rule the shift of the peak at ~22200 eV to the lower energies corresponds to the longer Ru-O distances in agreement with formation of Ru^{3+} phase, e.g. RuO(OH) [69].

Further quantitative analysis was performed with the Fourier transform (FT) analysis of the $k^2 \cdot \chi(k)$ data (Fig. 5B,C and S7, S8). At room temperature the signal from the both first and second coordination spheres of studied sample is similar to the one from RuO_2. Amplitude of the FT signal in the range of the first coordination sphere 0.8 … 2.0 Å (phase uncorrected) becomes smaller for elevated temperature and its maximum shifts toward larger values if compared to the RuO_2 reference. Additionally, in the region of 2.3 Å (phase uncorrected) the contribution from the Ru-Ru scattering in the metallic phase appears. Table 3 summarizes structural parameters for the Ru local coordination obtained during EXAFS fits (technical details of EXAFS analysis are reported in ESI).

At 100 °C and 5 MPa of H_2 the presence of Ru(III) was detected, the metallic phase started to form only at 100 °C, which was in agreement with H_2-TPR study (Fig. S6) and our previous results [31]; the final composition could be described as follows 65 % Ru(IV), 28 % RuOOH and 7 % Ru(0). At 200 °C, linear combination fitting calculated using theoretical spectra for different Ru species (0, I, III and IV), demonstrated the coexistence of three phases Ru(0), RuOOH and Ru(IV) in the 2Ru/TS-1 active catalyst in the following composition: 5 % Ru(IV), 45 % RuOOH and 50 % Ru(0). Therefore, the *in situ* and *ex situ* analysis of the spent catalysts demonstrated the formation of ruthenium hydrous oxide phase. However, the rapid transformation of Ru(IV) → Ru(0) in the hydrocarbon solution did not allow to detect the ruthenium hydrous oxide phase.

3.4. *The mechanism of guaiacol hydroconversion by in situ DRIFT analysis*

To establish the reaction mechanism, the hydrogenation of guaiacol over 2Ru/TS-1 catalyst was studied by *in situ* high-temperature DRIFT method (Fig. 6, S9-S12). The local environment of acid sites during the reaction was examined by analyzing the hydroxyl vibration (v(OH)) in the 3000–4000 cm^{-1} region of the DRIFT spectra, as presented in Fig. S9. Two bands centered at 3735 and 3520 cm^{-1}, were observed. The band at 3735 cm^{-1} is attributed to the stretching vibration of v(OH) in isolated Si-OH and Ti-OH groups, located both on the external surface and within the micropores of the TS-1 zeolite framework [70,71]. Medium strength and strong acid sites were not detected in the studied sample which is in agreement with NH_3-TPD and IR of adsorbed pyridine methods. The temperature increase from 200 to 250 °C revealed the weak acid sites involvement in the hydrodeoxygenation process. At 200 °C the concentration of silanol groups remain high, the gradual temperature raise to 225 °C and then to 250 °C leads to a sharp decrease of the silanol group concertation. The catalytic results in Table 2 suggest at 200 °C the main route is the aromatic ring saturation, while the hydrodeoxygenated products started to form at the elevated temperature. The saturation of guaiacol is a known exothermic process, with Gibbs free energy increasing from −18 (at 200 °C) to −10 (at 225 °C) to −2.5 kJ/mol (at 250 °C) [37]. In contrast, the Gibbs free energy for cyclohexanol formation decreases from −82 to −85 kJ/mol (200 – 250 °C), and for cyclohexanone formation, it decreases from −86 to −95 kJ/mol (200 – 250 °C) [37]. Consequently, an increase in temperature inevitably favors the formation of deoxygenated products. Following the saturation of the aromatic ring, several consecutive steps occur, including demethoxylation and hydrogenation, leading to the formation of cyclohexanone followed by the final C═O bond hydrogenation (Scheme 2). At 225 °C, the demethylation process becomes evident, as indicated by the appearance of a 1711 cm^{-1} band corresponding to the carbonyl group (Fig. 6), and a highly intense band at 1502 cm^{-1} attributed to conjugated -C═C-C═O bonds in an intermediate molecule [72]. The presence of a split intense band at 1380–1350 cm^{-1} suggests significant formation of cyclohexanol and 2-methoxycyclohexanol [73,74]. Additionally, the emergence of cyclohexane is detected by characteristic bands related to conformations at 828 cm^{-1} . At 250 °C, the maximum intensity of the band from the initial guaiacol is 3072, 1600, 777 cm^{-1} (Fig. 6) due to thermodynamic features of the process discussed above [37]. The intermediates in the process, as at 225°C, are predominantly ketones with a double bond within the cyclohexane ring, as indicated by bands at 1696 and 1509 cm^{-1} [75]. Additionally, bands at 1665 and 866 cm^{-1} suggest the presence of double bonds in the intermediates. The intense band at 823 cm^{-1} points to the predominant formation of cyclohexane in the "chair" conformation, while the band at 1217 cm^{-1} , associated with C-OH bond vibrations in cyclohexanol, further supports the identification of the alcohol. Cyclohexanol typically exhibits two prominent bands at 1360 and 1217 cm^{-1} [73,74]. However, at temperatures of 200–225 °C, the 1360 cm^{-1} band is more pronounced, while the 1217 cm^{-1} band appears with lower intensity. At 250 °C, the reverse is observed, with the 1217 cm^{-1} band becoming more intense and the 1362 cm^{-1} band decreasing in intensity. This behavior can be attributed to variations in the coordination of the cyclohexanol molecule on the catalyst surface.

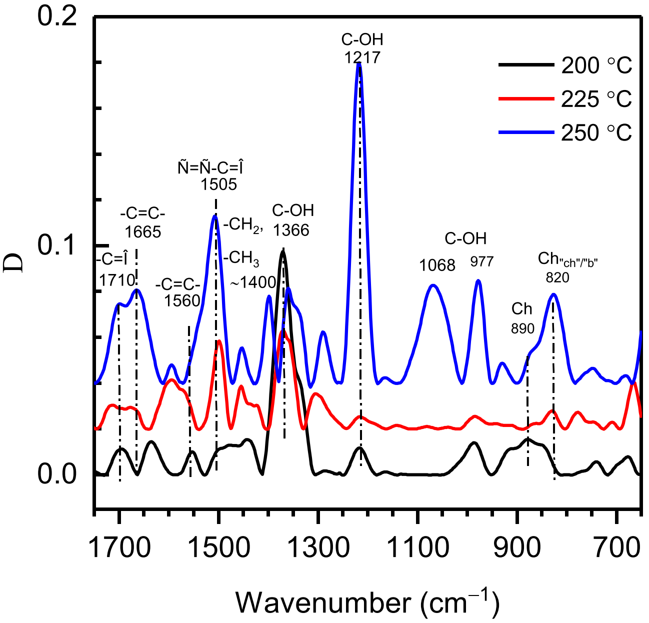

Fig. 6. Differential DRIFT spectra of Ru/TS-1 catalyst surface under a substrate and hydrogen flow at 200, 225 and 250 °C.

Table 3

Structural parameters obtained from EXAFS fit of in situ Ru K-edge spectra at room temperature and 200 °C in 5 MPa of H_2. At elevated temperature the XAS signal contains the contribution from two phases – metallic one and oxide, therefore reported coordination numbers are affected by the true Ru coordination and fraction of each phase.

Temperature	Scattering path	Coordination number	Distance, Å
25 °C	Ru-O	5.9	1.95
200 °C	Ru-O	3.0	2.11
	Ru-Ru (metal)	4.5	2.71
	Ru-Ru (oxide)	4.5	2.91

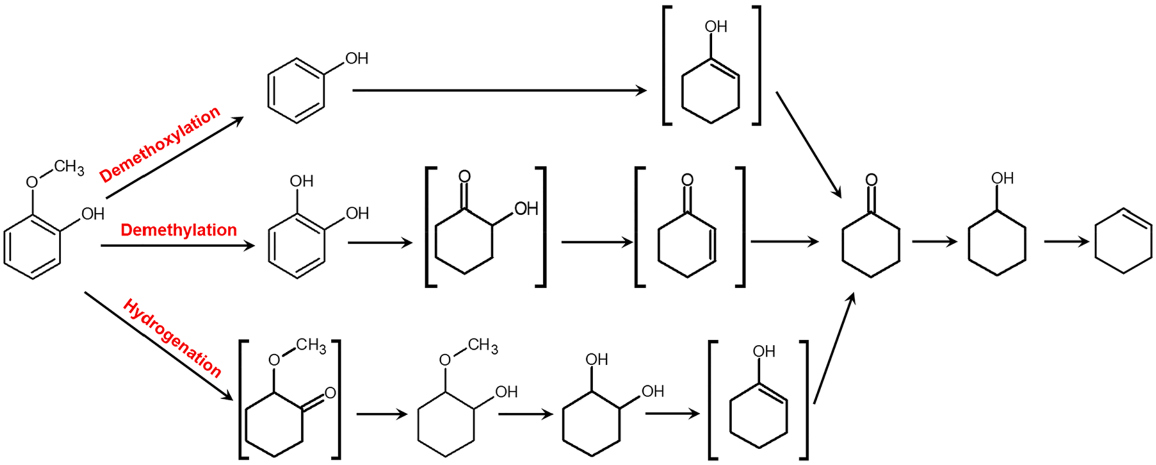

Scheme 2. General reaction pathways of guaiacol hydrogenation.

3.5. *Hydroprocessing in continuous-flow regime*

Three different conditions were tested to study the effect of temperature and LHSV on the BEA catalyst activity (Fig. 7). It should be noted that the pressure of H_2 was always kept at 5 MPa in order to be relevant during tandem process, even though H_2 does not directly interact with the substrate – cyclohexanol.

The resulting selectivity curves through time show that the elevated temperature increase the presence of side products – dimers of cyclohexene. Moreover, the catalyst deactivation occurs after 3 h of experiment (Fig. 7A). It is known that C–C coupling products can be observed when catalyzed by zeolites and not by mineral acids due to the fact that zeolite acid sites can stabilize the intermediates inside their pore system [76]. Although the deactivation of the catalysts occurs quite rapidly (200 °C, 5 MPa H_2, LHSV 1 h^{-1}), it can be seen that the conditions used in the experiment promote the formation of dimers (C12) to a greater extent than its dehydration to cyclohexene. This might open up a future research opportunity into valuable kerosene and diesel components. Isomers and light hydrocarbons (<C6) can be found as well as the side products. The mild conditions – 150 °C, 5 MPa H_2, LHSV 2.4 h^{-1} or 2.0 h^{-1} had beneficial effects on the catalytic stability and selectivity towards the desired products. The experiment performed during 12 h showed slight decrease in conversion at the end with a small increase in side products.

The results devoted to the hydrogenation of guaiacol are showed in Fig. 8. The hydroconversion of guaiacol is known to occur by three major processes [31,38,48]: (a) saturation of aromatic ring to form 2-methoxycyclohexanol (b) hydrogenolysis of –OCH_3 group to produce phenol, and (c) demethoxylation resulting in the formation of catechol (Scheme 2). All the routes can be further supplemented by hydrogenolysis to produce cyclohexanol. The most beneficial HDO mechanism of guaiacol is demethoxylation of -OCH_3 group, which also results in the production of phenol. It happens due to the fact that the bond dissociation energy of C(Ar)–OCH_3 (409–421 kJ/mol) compared to C(Ar)–OH (466 kJ/mol) in guaiacol [77,78]. When highly acidic catalysts are used, it is common to obtain a fully hydrogenated product - cyclohexane. [31, 79]; Therefore, in order to produce cyclohexanol efficiently, the catalyst and experimental conditions must be carefully adjusted. Three different temperatures, 150, 200 and 225 °C (Fig. 8 A-C), have been tested to discover the optimal conditions in terms of desired products distribution. It can be observed that an increase in temperature up to 225 °C had a favorable effect on the conversion of guaiacol over Ru/TS-1. At low temperature, fully hydrogenated product 2-methoxycyclohexanol was the main product. Further temperature increase enhances the selectivity towards HDO products. From a thermodynamic perspective, hydrogenation of aromatic ring is more advantageous way than the hydrogenolysis of C-O bond under the studied conditions [80]; therefore, the direct phenol formation is negligible at the expense of the fast cyclohexanol formation [81]. The bond dissociation energy of C(Ar)-O is more than 80 kJ/mole greater than C(sp^3)-O, which entails that the oxygen removal would be easier *via* hydrogenation step first [82]. Overall, increase in temperature from 150 °C to 225 °C had a positive

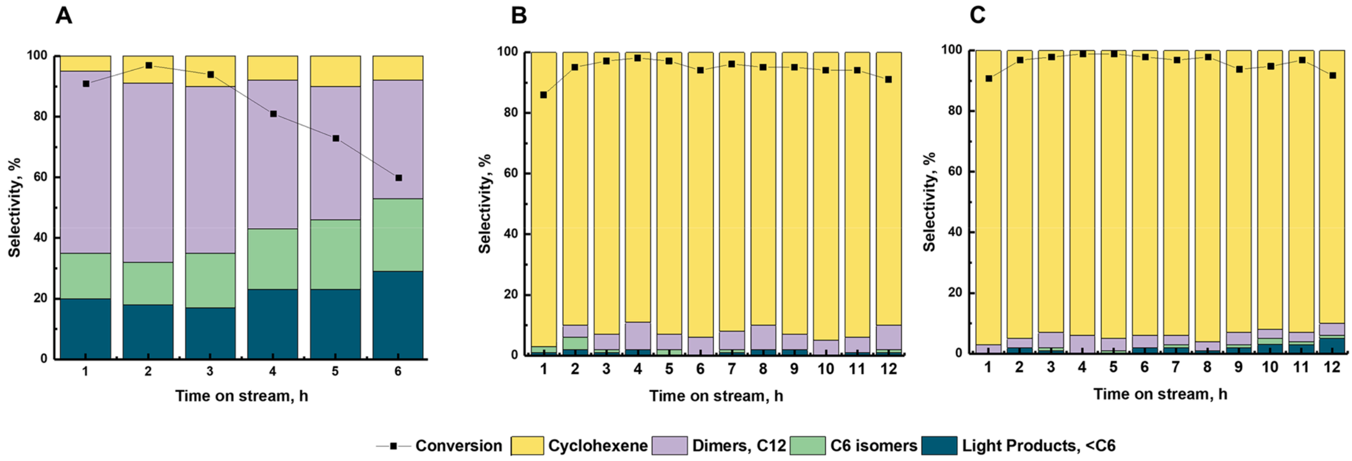

Fig. 7. Conversions and product distribution obtained in the DHA of cyclohexanol over BEA at (A) 200 °C, 5 MPa H_2, LHSV 1 h^{-1} (B) 150 °C, 5 MPa H_2, LHSV 2.4 h^{-1} and (C) 150 °C, 5 MPa H_2, LHSV 2 h^{-1}.

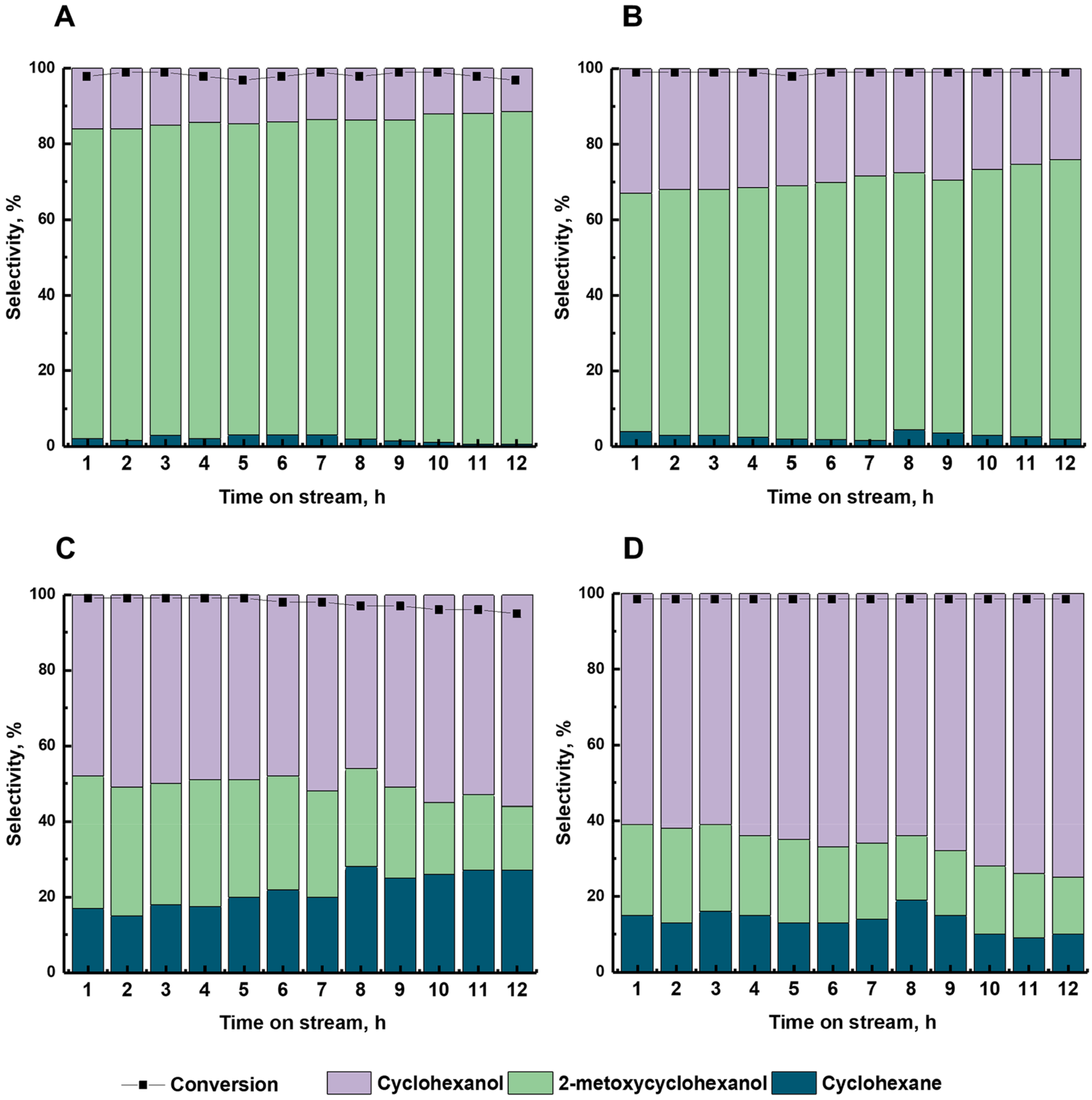

Fig. 8. Conversions and product distribution obtained in the HDO of guaiacol over 2Ru/TS-1 at (A) 150 °C, 5 MPa H_2, LHSV 2 h^{-1}, (B) 200 °C, 5 MPa H_2, LHSV 2 h^{-1}, (C) 225 °C, 5 MPa H_2, LHSV 2 h^{-1} and (D) 225 °C, 5 MPa H_2, LHSV 1.5 h^{-1}.

effect on the products distribution, which ranged from 18 % (at 150 °C) to 75 % (225 °C). At temperatures of 150 and 200 °C, the increase in selectivity towards cyclohexanol was accompanied by an enhancement in catalyst stability, which was evidenced by the absence of catalyst deactivation for 12 h on stream. The temperature increase from 200 to 225 °C is accompanied by an increase in selectivity towards cyclohexanol. The further conditions tuning by lowering LHSV allowed selecting optimal condition with the selectivity towards cyclohexanol up to 70 %. A possible reason for this observation is the increase of H_2 to substrate volume ratio, which resulted in a stable catalytic activity. The obtained results suggest that thermal effect has an enhancing impact on guaiacol conversion and cyclohexanol selectivity, which is consistent with the literature data [48,79,83].

The tandem process was run as follows: at the beginning, the 1st reactor with Ru/TS-1 catalyst was set under the optimized conditions bypassing the 2nd reactor with BEA catalyst. When the conversion of guaiacol became quantitative and the products distribution reached stable values, the corresponding valves were open to let the flow run through the 2nd reactor. Then the heater on the 2nd reactor was operated (160 °C) and approximately after 3 h on stream the tandem process was considered to launch. Evaluation of the long-term stability of the flow double-reactor setup with Ru/TS-1 and BEA catalysts at the more favored conditions (225 °C in the 1st reactor with Ru/TS-1, 160 °C in the 2nd reactor with BEA, 5 MPa H_2, LHSV 1.5 h^{-1}) took a 40 h catalytic test. As shown in Fig. 9, the tandem process demonstrates stable behavior during 32 h, which indicates that operational conditions have been set correctly. Moreover, the product distribution was stable on stream, with the selectivity towards targeted product cyclohexene up to 70 %. At the end of the run, the conversion of guaiacol decreased only to 95 wt%.

The coke formation of both catalysts after the 40 h catalytic run of tandem HDO – DHA was analyzed using differential TGA method (Fig. S15). Prior analysis, the both catalysts were dried at room temperature. The obtained results revealed that in the case of 2Ru/TS-1 catalyst there was no coke deposition since the highest temperature peak was at ~300 ºC which was associated with organic substrate that adsorbed on the catalyst. The 1st peak was observed under 100 ºC, it clearly belonged to the water obtained during HDO process. In the case of BEA catalyst, there were 3 distinctive peaks at ~140 ºC, 300 ºC and 550 ºC (water, adsorbed organic substances and carbon deposition

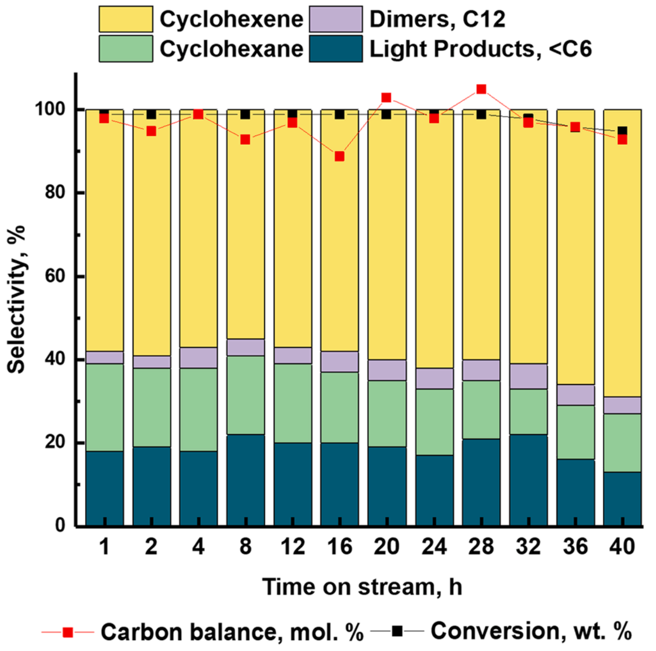

Fig. 9. Conversions and product distribution obtained in the tandem process HDO – DHA of guaiacol over 2Ru/TS-1 at 225 °C (HDO), 160 °C (DHA), 5 MPa H_2, LHSV 1.5 h^{-1};.

respectively) [84].

The catalytic results obtained in this study demonstrate that the developed process is comparable to the published data (Table 4). Moreover, the incorporation of a second reactor containing a dehydration catalyst (BEA) significantly enhances the selectivity towards cyclohexene.

3.6. Tandem conversion of bio-oil fraction into organosilicon compounds

The content of bio-oil was studied using 2D HSQC NMR, GC-MS and elemental (CHNS) analysis. The predominant group of components consists of carbohydrates, which account for over 30 % of the total composition. Significant quantities of lignin depolymerization products are also present, including monomeric units such as coniferyl, syringyl, and coumaric alcohols, along with their corresponding aldehydes and oligomers of varying molecular weights. Other compounds, including phenols, acids, and ketones, are present in lower concentrations, with their collective content not exceeding 10 %. Excluding water, which is not relevant for catalytic conversion, the bio-oil contains 37.2 % oxygen by weight. The H/C atomic ratio is 1.57, closely resembling that of heavy vacuum distillates or deasphaltized oils. However, the O/C atomic ratio is relatively low, at 0.58. In order to improve chemical and physical characteristics of bio-oil and to be able to run the bio-oil through the flow reactor, the extraction process was investigated using various solvents, including water, diethyl ether, dichloromethane, and *n*-hexane. The results are shown in Table S4-S5.

The most valuable fraction for the tandem hydroprocessing is the fraction extracted using dichloromethane. The composition of the initial bio-oil and extracted products can be resolved using combination of GC-MS and 2D HSQC NMR analysis (Table S5 and Fig. S13). The differences in signals intensity on 2D NMR spectra demonstrated that upon extraction with dichloromethane, the unsaturated functionalities such as phenols and other oxygen containing arenes were presented as dominating compounds. Though, carboxylic acids were not supposed to getting into this faction, such impurities were found in the extract (up to 1 wt%). After the extraction, the solvent was removed using rotary evaporator. Then the extract was dissolved in *n*-heptane (5 wt% for better solubility purposes) and fed into flow setup. The composition of the products are demonstrated in Table 5.

Although the hydrogenation of aromatics was complete, the DHA reaction proceeded only partially. Therefore, significant potential exists for further advancement in addressing this issue. The presence of carboxylic compounds in the extract could a challenge to Ru catalyst. Therefore, additional experiments in autoclave were performed in order to observe reactivation activity. The bio-oil fraction (5 wt% in *n*-heptane) was hydrogenated on 2Ru/TS-1 catalyst and after each cycle, the catalyst was removed from the mixture, dried and then calcined at 500 ºC. The activity of the catalyst after 4th cycle remained the same

Table 5
The products composition after tandem hydrogenation – dehydration over Ru/TS-1 and BEA catalysts (process conditions: 225 °C (HDO), 160 °C (DHA), 5 MPa H_2, LHSV 1.5 h^{-1}).

Compound	Content, wt%
Cyclohexene	57
alkylcyclohexene*	6
cyclohexanol	8
alkoxycyclohexanol*	7
cyclohexane	17
alkylcyclohexane*	5
Carbon balance	**93 %**

* alkyl – methyl, dimethyl, ethyl and propyl.

Table 4
Comparison of the catalytic activity in selective hydrogenation of oxygen-containing substances towards cyclohexene.

Catalyst type	Substrate, reaction conditions	Conversion, wt%	Main products	Selectivity (S) or Yield (Y) % of cyclohexene	Ref.
NiCu/ZrO_2	Guaiacol – dodecane, 300 °C; P(H_2) = 5.0 MPa; 8 h.	39	Toluene, cyclohexane	8 (S)	[85]
Rh/Si-Al aerogel	Guaiacol – decane/water, 250 °C; P(H_2) = 4.0 MPa; 1.5 h.	56	2-methoxycyclohexanol, cyclohexane	3.3 (S)	[86]
MoS_2/C	Guaiacol – dodecane, 300 °C; P(H_2) = 5.0 MPa; 5 h.	24	phenol	5 (S)	[87]
NiP_x	Guaiacol – decalin, 360 °C; P(H_2) = 6.0 MPa; 4 h.	77	Cyclohexene, cyclohexane	54 (S)	[88]
MoN-NH-ii	Guaiacol – decalin, 300 °C; P(H_2) = 5.0 MPa; 3 h	38	Phenol	7 (S)	[89]
MoS_2	Guaiacol, 300 °C; P(H_2) = 4.0 MPa;	HDO Conversion 20 %	cyclohexene	12 (S)	[90]
Ni/CNT	Guaiacol, 300 °C; P(H_2) = 5.0 MPa; 2 h	100	Cyclohexanol	18 (S)	[91]
NiCu/Al_2O_3	Guaiacol, 320 °C; P(H_2) = 17 MPa; 1 h	-	Cyclohexane	1.1 (Y)	[92]
Ni-Mo-S	Guaiacol – toluene - water, 360 °C; P(Syngas) = 5 MPa; 6 h	98	Cyclohexene, phenol	38 (S)	[32]
Ru/TS−1, BEA	Guaiacol – *n*-heptane, 225 °C, 5 MPa H_2, LHSV 1.5 h^{-1}	100	Cyclohexene	69 (S)	This work

(Fig. S14).

Hydrosilylation is the addition of hydrosilanes to unsaturated hydrocarbons usually using Pt-catalysts [51–54]. It is the main method used to produce organosilicon compounds, and one of the most widely applied atom-economical approach for functionalization of unsaturated hydrocarbons, mainly alkenes [51–54]. Organosilicon compounds find applications in virtually all areas of human activity, ranging from medicine and agriculture to construction and the aerospace industry. This reaction is extensively applied for the functionalization of terminal alkenes. However, hydrosilylation of internal alkenes is quite complicated due to their low reactivity. Still, some hydrosilylation products of internal alkenes, for example, cyclohexene [93–95], are used in industry and academia. Cyclohexyl-containing silanes are key components (external donors) in the composition of Ziegler–Natta catalysts [96,97]. Cyclohexyl-containing polysiloxanes feature a range of unique physico-chemical properties [98–100]. As discussed above, main product of bio-oil`s fraction processing is phenols, which can be transformed to cyclohexanol and then to cyclohexene. This final product obtained from bio-oil was used as cyclohexene source for the synthesis of cyclohexyl-containing silanes, using Pt-catalyzed hydrosilylation. For the hydrosilylation of cyclohexene fraction two hydrosilanes were chosen: one of the most widely used siloxy-derivetives – bis(trimethylsiloxy)methylsilane **1a**; and one of the most industrially important chlorosilane – di(chloro)methylsilane **1b** (Scheme 3).

Hydrosilylation proceeds effectively, despite low concentration of the reactant (cyclohexene) in this fraction, as well as the presence of impurities, which can participate side reactions with hydrosilane or poison Pt-catalyst. For example, reaction with hydrosilane **1a** allows obtaining of product **2a** in high yield (90 %). While using hydrosilane **1b**, a good yield (65 %) of corresponding product **2b** was also achieved. Reactions were carried out in the presence of industrial Karstedt's catalyst under relatively mild conditions (60 °C, 1 atm).

Mabrouk et al. analyzed economic aspects of a biorefinery process for catechol production from biomass [101]. It was shown that with total plant capital investment about ~5 million USD could allow a manufacturing capacity of 2.5 ton feedstock a day with valorization ratio of 3.02. In the other study devoted to hydroconversion of bio-oil the authors calculated the production of motor fuel from biomass with total capital investment of 726 million USD with the final gasoline price 1.6 USD per liter [102]. Assuming that the feedstock characteristics and technological parameters for biomass depolymerization, phenols extraction, and subsequent hydrotreating are comparable, the projected cost of cyclohexene would range from 3 to 6 USD per kilogram. Given that cyclohexene accounts for less than 5 % of the total cost of the final silicon-organic compound, dichloro-cyclohexyl-methylsilane, this cost structure enhances the economic feasibility of the proposed technology. The relatively low contribution of cyclohexene to the overall production cost supports the viability of integrating this process into industrial-scale silicon-organic synthesis, particularly in terms of reducing raw material expenses while maintaining competitive market pricing.

4. Conclusion

In this study, we demonstrated the possibility of bio-oil conversion into valuable chemicals. The catalytic performance was analysed by tuning the catalytic conditions of hydrodeoxygenation on Ru/TS-1 and dehydration on BEA zeolite. The tandem process conditions were optimized using model mixtures of phenolic compounds and saturated alcohol. The Ru on titanosilicate catalyst with weak Lewis acidity allowed to conduct highly selective hydrodeoxygenation of phenolic compounds from the real bio-oil to produce cyclohexanol (225 °C, 5 MPa H_2, LHSV 1.5 h^{-1}). The further simple dehydration reaction on BEA zeolite converted cyclohexanol to cyclohexene with high yield (160 °C, 5 MPa H_2, LHSV 1.5 h^{-1}). The obtained olefin fraction can be further transformed into valuable chemicals such as organosilicon compounds. The utilizing of the industrial Karstedt's catalyst under relatively mild conditions (60 °C, 1 atm) allowed acquiring the cyclohexyl-containing silanes in high yield (up to 90 %). In summary, a tandem process for the hydrogenation and dehydration of bio-oil-derived phenolic compounds into olefins was successfully developed. The results indicate an efficient strategy for the production of valuable chemicals from real bio-oils, offering new avenues for optimization in established biorefineries.

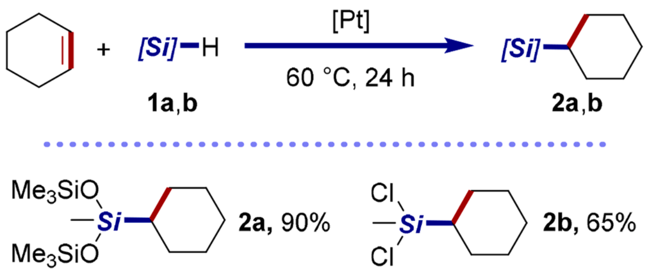

Scheme 3. Cyclohexene hydrosilylation using Pt catalyst.

Funding

The authors acknowledge the Ministry of Science and Higher Education of the Russian Federation for financial support (Agreement no. 075-15-2023-583).

CRediT authorship contribution statement

Zhongyang Luo: Writing – review & editing, Conceptualization. **Evgeny Naranov:** Writing – review & editing, Writing – original draft, Supervision, Project administration, Funding acquisition. **Anton Maximov:** Writing – review & editing, Conceptualization. **Alexey Sadovnikov:** Writing – original draft, Methodology, Investigation. **Olga Arapova:** Writing – original draft, Methodology, Investigation. **Alexander Guda:** Investigation, Formal analysis. **Konstantin Dementev:** Writing – review & editing, Investigation. **Ashot Arzumanyan:** Investigation. **Gleb Kubrin:** Investigation. **Dmitry Kholodkov:** Investigation. **Alexander Zagrebaev:** Investigation. **Kaige Wang:** Writing – review & editing, Conceptualization.

Declaration of Competing Interest

The authors declare that they have no known competing financial interests or personal relationships that could have appeared to influence the work reported in this paper.

Acknowledgment

This work was performed using the equipment of the Shared Research Center «Analytical center of deep oil processing and petrochemistry of TIPS RAS. The authors thank A.V. Shubnikov Institute of Crystallography RAS for TEM analysis. The SEM analysis was performed using the equipment of the JRC PMR IGIC RAS.

Appendix A. Supporting information

Supplementary data associated with this article can be found in the online version at doi:10.1016/j.jece.2024.115050.

Data availability

Data will be made available on request.

References

[1] K. Jacobson, K.C. Maheria, A. Kumar Dalai, Bio-oil valorization: a review, Renew. Sustain. Energy Rev. 23 (2013) 91–106, https://doi.org/10.1016/j.rser.2013.02.036.

[2] S. Xiu, A. Shahbazi, Bio-oil production and upgrading research: a review, Renew. Sustain. Energy Rev. 16 (2012) 4406–4414, https://doi.org/10.1016/j.rser.2012.04.028.

[3] L. Machineni, G. Rao Anupoju, Review on valorization of lignocellulosic biomass for green plastics production: sustainable and cleaner approaches, Sustain. Energy Technol. Assess. 53 (2022) 102698, https://doi.org/10.1016/j.seta.2022.102698.

[4] G.Q. Chen, M.K. Patel, Plastics derived from biological sources: present and future: a technical and environmental review, Chem. Rev. 112 (2012) 2082–2099, https://doi.org/10.1021/cr200162d.

[5] H. Golmohamadi, Demand-side management in industrial sector: a review of heavy industries, Renew. Sustain. Energy Rev. 156 (2022) 111963, https://doi.org/10.1016/j.rser.2021.111963.

[6] Y. Xu, Z. Lun, Z. Pan, H. Wang, X. Zhou, C. Zhao, D. Zhang, Occurrence space and state of shale oil: a review, J. Pet. Sci. Eng. 211 (2022) 110183, https://doi.org/10.1016/j.petrol.2022.110183.

[7] C. Dhoke, A. Zaabout, S. Cloete, S. Amini, Review on reactor configurations for adsorption-based CO2 capture, Ind. Eng. Chem. Res. 60 (2021) 3779–3798, https://doi.org/10.1021/acs.iecr.0c04547.

[8] L. Fu, Z. Ren, W. Si, Q. Ma, W. Huang, K. Liao, Z. Huang, Y. Wang, J. Li, P. Xu, Research progress on CO2 capture and utilization technology, J. CO2 Util. 66 (2022) 102260, https://doi.org/10.1016/j.jcou.2022.102260.

[9] M. Hanifa, R. Agarwal, U. Sharma, P.C. Thapliyal, L.P. Singh, A review on CO2capture and sequestration in the construction industry: emerging approaches and commercialised technologies, J. CO2 Util. 67 (2023) 102292, https://doi.org/10.1016/j.jcou.2022.102292.

[10] S.G. Zlotin, K.S. Egorova, V.P. Ananikov, A.A. Akulov, M.V. Varaksin, O. N. Chupakhin, V.N. Charushin, K.P. Bryliakov, A.D. Averin, I.P. Beletskaya, E. L. Dolengovski, Y.H. Budnikova, O.G. Sinyashin, Z.N. Gafurov, A.O. Kantyukov, D.G. Yakhvarov, A.V. Aksenov, M.N. Elinson, V.G. Nenajdenko, A.M. Chibiryaev, N.S. Nesterov, E.A. Kozlova, O.N. Martyanov, I.A. Balova, V.N. Sorokoumov, D. A. Guk, E.K. Beloglazkina, D.A. Lemenovskii, I.Y. Chukicheva, L.L. Frolova, E. S. Izmest'ev, I.A. Dvornikova, A.V. Popov, A.V. Kutchin, D.M. Borisova, A. A. Kalinina, A.M. Muzafarov, I.V. Kuchurov, A.L. Maximov, A.V. Zolotukhina, The green chemistry paradigm in modern organic synthesis, Russ. Chem. Rev. 92 (2023) RCR5104, https://doi.org/10.59761/rcr5104.

[11] C.-H. Huang, C.-S. Tan, A review: CO2 utilization, Aerosol Air Qual. Res. 14 (2014) 480–499, https://doi.org/10.4209/aaqr.2013.10.0326.

[12] W.Y. Hong, A techno-economic review on carbon capture, utilisation and storage systems for achieving a net-zero CO2 emissions future, Carbon Capture Sci. Technol. 3 (2022) 100044, https://doi.org/10.1016/j.ccst.2022.100044.

[13] F. Meng, Y. Meng, T. Ju, S. Han, L. Lin, J. Jiang, Research progress of aqueous amine solution for CO2 capture: a review, Renew. Sustain. Energy Rev. 168 (2022) 112902, https://doi.org/10.1016/j.rser.2022.112902.

[14] A.G. Olabi, M.A. Abdelkareem, Renewable energy and climate change, Renew. Sustain. Energy Rev. 158 (2022) 112111, https://doi.org/10.1016/j.rser.2022.112111.

[15] I. Gunnarsdottir, B. Davidsdottir, E. Worrell, S. Sigurgeirsdottir, Sustainable energy development: history of the concept and emerging themes, Renew. Sustain. Energy Rev. 141 (2021) 110770, https://doi.org/10.1016/j.rser.2021.110770.

[16] B. Nastasi, N. Markovska, T. Puksec, N. Duić, A. Foley, Renewable and sustainable energy challenges to face for the achievement of sustainable development goals, Renew. Sustain. Energy Rev. 157 (2022) 112071, https://doi.org/10.1016/j.rser.2022.112071.

[17] K. Moustakas, M. Loizidou, M. Rehan, A.S. Nizami, A review of recent developments in renewable and sustainable energy systems: key challenges and future perspective, Renew. Sustain. Energy Rev. 119 (2020) 109418, https://doi.org/10.1016/j.rser.2019.109418.

[18] H.A. Baloch, S. Nizamuddin, M.T.H. Siddiqui, S. Riaz, A.S. Jatoi, D.K. Dumbre, N. M. Mubarak, M.P. Srinivasan, G.J. Griffin, Recent advances in production and upgrading of bio-oil from biomass: a critical overview, J. Environ. Chem. Eng. 6 (2018) 5101–5118, https://doi.org/10.1016/j.jece.2018.07.050.

[19] Z. Luo, Q. Qian, H. Sun, Q. Wei, J. Zhou, K. Wang, Lignin-first biorefinery for converting lignocellulosic biomass into fuels and chemicals, Energies 16 (2023) 125, https://doi.org/10.3390/en16010125.

[20] S. Wang, G. Dai, H. Yang, Z. Luo, Lignocellulosic biomass pyrolysis mechanism: a state-of-the-art review, Prog. Energy Combust. Sci. 62 (2017) 33–86, https://doi.org/10.1016/j.pecs.2017.05.004.

[21] C. Wang, T. Li, W. Xu, S. Wang, K. Wang, Recent advances in co-processing biomass feedstock with petroleum feedstock: a review, Front. Energy (2024) 1–25, https://doi.org/10.1007/s11708-024-0920-1.

[22] K. Wang, D.C. Dayton, J.E. Peters, O.D. Mante, Reactive catalytic fast pyrolysis of biomass to produce high-quality bio-crude, Green. Chem. 19 (2017) 3243–3251, https://doi.org/10.1039/c7gc01088e.

[23] K. Wang, K.H. Kim, R.C. Brown, Catalytic pyrolysis of individual components of lignocellulosic biomass, Green. Chem. 16 (2014) 727–735, https://doi.org/10.1039/c3gc41288a.

[24] E.R. Naranov, K.I. Dement'ev, I.M. Gerzeliev, N.V. Kolesnichenko, E. A. Roldugina, A.L. Maksimov, The role of zeolite catalysis in modern petroleum refining: contribution from domestic technologies, Pet. Chem. 59 (2019), https://doi.org/10.1134/S0965544119030101.

[25] D. Chen, J. Zhou, Q. Zhang, X. Zhu, Evaluation methods and research progresses in bio-oil storage stability, Renew. Sustain. Energy Rev. 40 (2014) 69–79, https://doi.org/10.1016/j.rser.2014.07.159.

[26] J. Cai, M.M. Rahman, S. Zhang, M. Sarker, X. Zhang, Y. Zhang, X. Yu, E.H. Fini, Review on aging of bio-oil from biomass pyrolysis and strategy to slowing aging, Energy Fuels 35 (2021) 11665–11692, https://doi.org/10.1021/acs.energyfuels.1c01214.

[27] B.J. Alvarez-Chavez, S. Godbout, J.H. Palacios-Rios, É . Le Roux, V. Raghavan, Physical, chemical, thermal and biological pre-treatment technologies in fast pyrolysis to maximize bio-oil quality: a critical review, Biomass. Bioenergy 128 (2019) 105333, https://doi.org/10.1016/j.biombioe.2019.105333. É.

[28] C. Lindfors, E. Kuoppala, A. Oasmaa, Y. Solantausta, V. Arpiainen, Fractionation of bio-oil, Energy Fuels 28 (2014) 5785–5791, https://doi.org/10.1021/ef500754d.

[29] N.L. Panwar, A.S. Paul, An overview of recent development in bio-oil upgrading and separation techniques, Environ. Eng. Res 26 (2021) 0–1, https://doi.org/10.4491/eer.2020.382.

[30] A.A. Kiss, J.P. Lange, B. Schuur, D.W.F. Brilman, A.G.J. van der Ham, S.R. A. Kersten, Separation technology–making a difference in biorefineries, Biomass. Bioenergy 95 (2016) 296–309, https://doi.org/10.1016/J.BIOMBIOE.2016.05.021.

[31] E. Naranov, A. Sadovnikov, O. Arapova, T. Kuchinskaya, O. Usoltsev, A. Bugaev, K. Janssens, D. De Vos, A. Maximov, The in-situ formation of supported hydrous ruthenium oxide in aqueous phase during HDO of lignin-derived fractions, Appl. Catal. B Environ. 334 (2023) 122861, https://doi.org/10.1016/j.apcatb.2023.122861.

[32] A.V. Vutolkina, I.G. Baigildin, A.P. Glotov, A.A. Pimerzin, A.V. Akopyan, A. L. Maximov, E.A. Karakhanov, Hydrodeoxygenation of guaiacol via in situ H2 generated through a water gas shift reaction over dispersed NiMoS catalysts from oil-soluble precursors: tuning the selectivity towards cyclohexene, Appl. Catal. B Environ. 312 (2022) 121403, https://doi.org/10.1016/j.apcatb.2022.121403.

[33] M. Ozagac, C. Bertino-Ghera, D. Uzio, A. Quignard, D. Laurenti, C. Geantet, Catalytic hydroconversion of pyrolytic bio-oil: understanding and limiting macromolecules formation, Biomass. Bioenergy 108 (2018) 501–510, https://doi.org/10.1016/j.biombioe.2017.10.002.

[34] Y. Shi, E. Xing, K. Wu, J. Wang, M. Yang, Y. Wu, Recent progress on upgrading of bio-oil to hydrocarbons over metal/zeolite bifunctional catalysts, Catal. Sci. Technol. 7 (2017) 2385–2415, https://doi.org/10.1039/c7cy00574a.

[35] X. Li, G. Chen, C. Liu, W. Ma, B. Yan, J. Zhang, Hydrodeoxygenation of lignin-derived bio-oil using molecular sieves supported metal catalysts: a critical review, Renew. Sustain. Energy Rev. 71 (2017) 296–308, https://doi.org/10.1016/j.rser.2016.12.057.

[36] A.H. Zacher, M.V. Olarte, D.M. Santosa, D.C. Elliott, S.B. Jones, A review and perspective of recent bio-oil hydrotreating research, Green. Chem. 16 (2014) 491–515, https://doi.org/10.1039/c3gc41382a.

[37] E.R. Naranov, A.A. Sadovnikov, O.V. Arapova, A.L. Bugaev, O.A. Usoltsev, D. N. Gorbunov, V. Russo, D.Y. Murzin, A.L. Maximov, Mechanistic insights on Ru nanoparticle in situ formation during hydrodeoxygenation of lignin-derived substances to hydrocarbons, Catal. Sci. Technol. 13 (2023) 1571–1583, https://doi.org/10.1039/D2CY01127A.

[38] G. Jiang, Y. Hu, G. Xu, X. Mu, H. Liu, Controlled hydrodeoxygenation of phenolic components in pyrolysis bio-oil to arenes, ACS Sustain. Chem. Eng. 6 (2018) 5772–5783, https://doi.org/10.1021/acssuschemeng.7b03276.

[39] E.A. Roldugina, E.R. Naranov, A.L. Maximov, E.A. Karakhanov, Hydrodeoxygenation of guaiacol as a model compound of bio-oil in methanol over mesoporous noble metal catalysts, Appl. Catal. A Gen. 553 (2018) 24–35, https://doi.org/10.1016/j.apcata.2018.01.008.

[40] F. Huang, W. Li, Q. Lu, X. Zhu, Homogeneous catalytic hydrogenation of bio-oil and related model aldehydes with RuCl2(PPh3)3, Chem. Eng. Technol. 33 (2010) 2082–2088, https://doi.org/10.1002/ceat.201000229.

[41] L. Busetto, D. Fabbri, R. Mazzoni, M. Salmi, C. Torri, V. Zanotti, Application of the Shvo catalyst in homogeneous hydrogenation of bio-oil obtained from pyrolysis of white poplar: new mild upgrading conditions, Fuel 90 (2011) 1197–1207, https://doi.org/10.1016/j.fuel.2010.10.036.

[42] A. Gil, I. Sancho-Sanz, S.A. Korili, Progress and perspectives in the catalytic hydrotreatment of bio-oils: effect of the nature of the metal catalyst, Ind. Eng. Chem. Res. 63 (2024) 11759–11775, https://doi.org/10.1021/acs.iecr.4c00747.

[43] E. Naranov, Sustainable production of chemicals via hydrotreating of CO 2 and biomass derived molecules using heterogeneous noble metal oxide catalysts, ChemCatChem 16 (2024), https://doi.org/10.1002/cctc.202301268.

[44] R. Shu, B. Lin, J. Zhang, C. Wang, Z. Yang, Y. Chen, Efficient catalytic hydrodeoxygenation of phenolic compounds and bio-oil over highly dispersed Ru/TiO2, Fuel Process. Technol. 184 (2019) 12–18, https://doi.org/10.1016/j.fuproc.2018.11.004.

[45] Z. Ma, L. Wei, W. Zhou, L. Jia, B. Hou, D. Li, Y. Zhao, Upgrading of fast pyrolysis bio-oil to drop-in fuel over Ru catalysts, J. Energy Inst. 92 (2019) 855–860, https://doi.org/10.1016/j.joei.2018.06.013.

[46] A. Sanna, T.P. Vispute, G.W. Huber, Hydrodeoxygenation of the aqueous fraction of bio-oil with Ru/C and Pt/C catalysts, Appl. Catal. B Environ. 165 (2015) 446–456, https://doi.org/10.1016/j.apcatb.2014.10.013.

[47] X. Zhang, W. Tang, Q. Zhang, Y. Li, L. Chen, Y. Xu, C. Wang, L. Ma, Production of hydrocarbon fuels from heavy fraction of bio-oil through hydrodeoxygenative upgrading with Ru-based catalyst, Fuel 215 (2018) 825–834, https://doi.org/10.1016/j.fuel.2017.11.111.

[48] A. Kumar, B. Thallada, Hydrodeoxygenation of lignin derived phenolics over a hydrous ruthenium oxide based catalyst(s): role of surface water molecules and acidity of the support, Sustain. Energy Fuels. 5 (2021) 3802–3817, https://doi.org/10.1039/d1se00102g.

[49] Z. Luo, Y. Wang, M. He, C. Zhao, Precise oxygen scission of lignin derived aryl ethers to quantitatively produce aromatic hydrocarbons in water, Green. Chem. 18 (2016) 433–441, https://doi.org/10.1039/c5gc01790d.

[50] J. Shangguan, A.J.R. Hensley, M.V. Gradiski, N. Pfriem, J.S. McEwen, R. H. Morris, Y.H.C. Chin, The role of protons and hydrides in the catalytic hydrogenolysis of guaiacol at the ruthenium nanoparticle-water interface, ACS Catal. 10 (2020) 12310–12332, https://doi.org/10.1021/acscatal.0c01963.

[51] I.K. Goncharova, I.P. Beletskaya, A.V. Arzumanyan, Prospects in sustainable hydrosilylation by biphase catalysis, ChemCatChem 16 (2024) e202400155, https://doi.org/10.1002/cctc.202400155.

[52] L.D. de Almeida, H. Wang, K. Junge, X. Cui, M. Beller, Recent advances in catalytic hydrosilylations, Dev. Beyond Tradit. Platin. Angew. Chem. Int. Ed. 60 (2021) 550–565, https://doi.org/10.1002/anie.202008729.

[53] J.V. Obligacion, P.J. Chirik, Earth-abundant transition metal catalysts for alkene hydrosilylation and hydroboration, Nat. Rev. Chem. 2 (2018) 15–34, https://doi.org/10.1038/s41570-018-0001-2.

[54] B. Marciniec, Functionalised (Poly)silsesquioxanes and Silicon-containing Dendrimers. Hydrosilylation, Springer, Dordrecht, 2008, pp. 215–240, https://doi.org/10.1007/978-1-4020-8172-9_7.

[55] Q. Du, Y. Guo, H. Duan, H. Li, Y. Chen, H. Liu, Synthesis of hierarchical TS-1 zeolite via a novel three-step crystallization method and its excellent catalytic performance in oxidative desulfurization, Fuel 188 (2017) 232–238, https://doi.org/10.1016/j.fuel.2016.10.045.

[56] P.V. Shvets, P.A. Prokopovich, A.I. Dolgoborodov, O.A. Usoltsev, A.A. Skorynina, E.G. Kozyr, V.V. Shapovalov, A.A. Guda, A.L. Bugaev, E.R. Naranov, D. N. Gorbunov, K. Janssens, D.E. De Vos, A.L. Trigub, E. Fonda, M.B. Leshchinsky, V.R. Zagackij, A.V. Soldatov, A.Y. Goikhman, In Situ X-ray absorption spectroscopy cells for high pressure homogeneous catalysis, Catalysts 12 (2022) 1264, https://doi.org/10.3390/catal12101264.

[57] Y. Han, A.P. Pinheiro Pires, M. Denson, A.G. McDonald, M. Garcia-Perez, Ternary phase diagram of water/bio-oil/organic solvent for bio-oil fractionation, Energy Fuels 34 (2020) 16250–16264, https://doi.org/10.1021/acs.energyfuels.0c03100.

[58] B.D. Karstedt, Platinum complexes of unsaturated siloxanes and platinum containing organopolysiloxanes, US3775452A, 1973.

[59] M. Kruk, M. Jaroniec, Y. Sakamoto, O. Terasaki, R. Ryoo, C.H. Ko, Determination of pore size and pore wall structure of mcm-41 by using nitrogen adsorption, transmission electron microscopy, and x-ray diffraction, J. Phys. Chem. B. 104 (2000) 292–301, https://doi.org/10.1021/jp992718a.

[60] M. Tamura, K. Shimizu, A. Satsuma, Comprehensive IR study on acid/base properties of metal oxides, Appl. Catal. A Gen. 433–434 (2012) 135–145, https://doi.org/10.1016/j.apcata.2012.05.008.

[61] B. Ravel, M. Newville, Athena, artemis, hephaestus: data analysis for X-ray absorption spectroscopy using IFEFFIT, J. Synchrotron Radiat. (2005) 537–541, https://doi.org/10.1107/S0909049505012719.

[62] A. Silvestre-Albero, A. Grau-Atienza, E. Serrano, J. García-Martínez, J. Silvestre-Albero, Desilication of TS-1 zeolite for the oxidation of bulky molecules, Catal. Commun. 44 (2014) 35–39, https://doi.org/10.1016/j.catcom.2013.08.004.

[63] A. Carati, C. Flego, E. Previde Massara, R. Millini, L. Carluccio, W. Parker, G. Bellussi, Stability of Ti in MFI and Beta structures: a comparative study, Microporous Mesoporous Mater. 30 (1999) 137–144, https://doi.org/10.1016/S1387-1811(99)00018-9.

[64] M. Shakeri, S.B. Dehghanpour, Rational synthesis of TS-1 zeolite to direct both particle size and framework Ti in favor of enhanced catalytic performance, Microporous Mesoporous Mater. 298 (2020) 110066, https://doi.org/10.1016/j.micromeso.2020.110066.

[65] G. Ricchiardi, A. Damin, S. Bordiga, C. Lamberti, G. Spanò, F. Rivetti, A. Zecchina, Vibrational structure of titanium silicate catalysts. a spectroscopic and theoretical study, J. Am. Chem. Soc. 123 (2001) 11409–11419, https://doi.org/10.1021/ja010607v.

[66] X. Ma, J. Gong, S. Wang, F. He, H. Guo, X. Yang, G. Xu, Characterization and reactivity of stannum modified titanium silicalite TS-1 catalysts for transesterification of dimethyl oxalate with phenol, J. Mol. Catal. A Chem. 237 (2005) 1–8, https://doi.org/10.1016/j.molcata.2005.04.052.

[67] X. Ma, H. Guo, S. Wang, Y. Sun, Transesterification of dimethyl oxalate with phenol over TS-1 catalyst, Fuel Process. Technol. 83 (2003) 275–286, https://doi.org/10.1016/S0378-3820(03)00075-4.

[68] X. Wang, S. Zhu, S. Wang, Y. He, Y. Liu, J. Wang, W. Fan, Y. Lv, Low temperature hydrodeoxygenation of guaiacol into cyclohexane over Ni/SiO 2 catalyst combined with Hβ zeolite, RSC Adv. 9 (2019) 3868–3876, https://doi.org/10.1039/C8RA09972C.

[69] C.R. Natoli, Distance dependence of continuum and bound state of excitonic resonances in x-ray absorption near edge structure (XANES), in: Distance Dependence of Continuum and Bound State of Excitonic Resonances in X-Ray Absorption Near Edge Structure (XANES), Springer, Berlin, Heidelberg, 1984, pp. 38–42, https://doi.org/10.1007/978-3-642-46522-2_10.

[70] F. Yi, Y. Chen, Z. Tao, C. Hu, X. Yi, A. Zheng, X. Wen, Y. Yun, Y. Yang, Y. Li, Origin of weak Lewis acids on silanol nests in dealuminated zeolite Beta, J. Catal. 380 (2019) 204–214, https://doi.org/10.1016/j.jcat.2019.10.008.

[71] W. Wu, D.T. Tran, S. Cheng, Y. Zhang, N. Li, H. Chen, Y.-H. (Cathy) Chin, L. Yao, D. Liu, Local environment and catalytic property of external lewis acid sites in hierarchical lamellar titanium Silicalite-1 zeolites, Microporous Mesoporous Mater. 311 (2021) 110710, https://doi.org/10.1016/j.micromeso.2020.110710.

[72] T. Förster, Chemical Applications of Spectroscopy, von W. West. (Technique of Organic Chemistry, Vol. IX. Herausgeber A. Weissberger). Interscience Publishers, New York 1956. 1. Aufl., XXIV, 787 S., geb. $ 15. —, John Wiley & Sons, Ltd, 1957. https://doi.org/10.1002/ANGE.19570692219.

[73] P.M. de Souza, R.C. Rabelo-Neto, L.E.P. Borges, G. Jacobs, B.H. Davis, T. Sooknoi, D.E. Resasco, F.B. Noronha, Role of keto intermediates in the hydrodeoxygenation of phenol over Pd on oxophilic supports, ACS Catal. 5 (2015) 1318–1329, https://doi.org/10.1021/cs501853t. Vis, T. Sooknoi, D.e. Resasco, F.b. Noronha, Role of Keto Intermediates in the.

[74] V. Fridman, Dehydrogenation of cyclohexanol on copper-containing catalysts II. The pathways of the cyclohexanol dehydrogenation reaction to cyclohexanone on copper-active sites in oxidation state Cu0 and Cu+, J. Catal. 222 (2004) 545–557, https://doi.org/10.1016/j.jcat.2003.12.016.

[75] G.S. Foo, A.K. Rogers, M.M. Yung, C. Sievers, Steric effect and evolution of surface species in the hydrodeoxygenation of bio-oil model compounds over Pt/HBEA, ACS Catal. 6 (2016) 1292–1307, https://doi.org/10.1021/acscatal.5b02684.

[76] A. Vjunov, M.Y. Hu, J. Feng, D.M. Camaioni, D. Mei, J.Z. Hu, C. Zhao, J. A. Lercher, Following solid-acid-catalyzed reactions by MAS NMR spectroscopy in liquid phase - Zeolite-catalyzed conversion of cyclohexanol in water, Angew. Chem. Int. Ed. 53 (2014) 479–482, https://doi.org/10.1002/anie.201306673.

[77] Y.-R. Luo, Comprehensive Handbook of Chemical Bond Energies, CRC Press, 2007, https://doi.org/10.1201/9781420007282.

[78] Z. Luo, Z. Zheng, Y. Wang, G. Sun, H. Jiang, C. Zhao, Hydrothermally stable Ru/HZSM-5-catalyzed selective hydrogenolysis of lignin-derived substituted phenols to bio-arenes in water, Green. Chem. 18 (2016) 5845–5858, https://doi.org/10.1039/c6gc01971d.

[79] W. Zhang, J. Chen, R. Liu, S. Wang, L. Chen, K. Li, Hydrodeoxygenation of lignin-derived phenolic monomers and dimers to alkane fuels over bifunctional zeolite-supported metal catalysts, ACS Sustain. Chem. Eng. 2 (2014) 683–691, https://doi.org/10.1021/sc400401n.

[80] A. Sulman, P. Mäki-Arvela, L. Bomont, M. Alda-Onggar, V. Fedorov, V. Russo, K. Eränen, M. Peurla, U. Akhmetzyanova, L. Skuhrovcová, Z. Tišler, H. Grénman, J. Wärnå, D.Y. Murzin, Kinetic and thermodynamic analysis of guaiacol hydrodeoxygenation, Catal. Lett. 149 (2019) 2453–2467, https://doi.org/10.1007/s10562-019-02856-x.

[81] M. Ishikawa, M. Tamura, Y. Nakagawa, K. Tomishige, Demethoxylation of guaiacol and methoxybenzenes over carbon-supported Ru–Mn catalyst, Appl. Catal. B Environ. 182 (2016) 193–203, https://doi.org/10.1016/j.apcatb.2015.09.021.

[82] E. Furimsky, Catalytic hydrodeoxygenation, Appl. Catal. A Gen. 199 (2000) 147–190, https://doi.org/10.1016/S0926-860X(99)00555-4.

[83] W. Luo, W. Cao, P.C.A. Bruijnincx, L. Lin, A. Wang, T. Zhang, Zeolite-supported metal catalysts for selective hydrodeoxygenation of biomass-derived platform molecules, Green. Chem. 21 (2019) 3744–3768, https://doi.org/10.1039/c9gc01216h.

[84] M. Koehle, R.F. Lobo, Lewis acidic zeolite beta catalyst for the meerwein-ponndorf-verley reduction of furfural, Catal. Sci. Technol. 6 (2016) 3018–3026, https://doi.org/10.1039/c5cy01501d.

[85] X. Zhang, T. Wang, L. Ma, Q. Zhang, Y. Yu, Q. Liu, Characterization and catalytic properties of Ni and NiCu catalysts supported on ZrO2–SiO2 for guaiacol hydrodeoxygenation, Catal. Commun. 33 (2013) 15–19, https://doi.org/10.1016/j.catcom.2012.12.011.

[86] J.S. Yoon, J. Choi, D.J. Suh, K. Lee, H. Lee, J. Ha, Water-assisted selective hydrodeoxygenation of lignin-derived guaiacol to monooxygenates, ChemCatChem 7 (2015) 2669–2674, https://doi.org/10.1002/cctc.201500345.

[87] S. Mukundan, M. Konarova, L. Atanda, Q. Ma, J. Beltramini, Guaiacol hydrodeoxygenation reaction catalyzed by highly dispersed, single layered MoS 2 /C, Catal. Sci. Technol. 5 (2015) 4422–4432, https://doi.org/10.1039/C5CY00607D.

[88] M.A. Golubeva, A.L. Maximov, Catalytic system based on nickel(II) acetate and hypophosphorous acid for the selective hydrodeoxygenation of guaiacol, Mendeleev Commun. 29 (2019) 550–552, https://doi.org/10.1016/j.mencom.2019.09.024.

[89] I.T. Ghampson, C. Sepúlveda, R. Garcia, B.G. Frederick, M.C. Wheeler, N. Escalona, W.J. DeSisto, Guaiacol transformation over unsupported molybdenum-based nitride catalysts, Appl. Catal. A Gen. 413–414 (2012) 78–84, https://doi.org/10.1016/j.apcata.2011.10.050.

[90] V.N. Bui, D. Laurenti, P. Afanasiev, C. Geantet, Hydrodeoxygenation of guaiacol with CoMo catalysts. Part I: promoting effect of cobalt on HDO selectivity and activity, Appl. Catal. B Environ. 101 (2011) 239–245, https://doi.org/10.1016/j.apcatb.2010.10.025.

[91] A.B. Dongil, L. Pastor-Pérez, A. Sepúlveda-Escribano, R. García, N. Escalona, Hydrodeoxygenation of guaiacol: tuning the selectivity to cyclohexene by introducing Ni nanoparticles inside carbon nanotubes, Fuel 172 (2016) 65–69, https://doi.org/10.1016/j.fuel.2016.01.002.

[92] M.V. Bykova, D.Y. Ermakov, V.V. Kaichev, O.A. Bulavchenko, A.A. Saraev, M. Y. Lebedev, V.A Yakovlev, Ni-based sol–gel catalysts as promising systems for crude bio-oil upgrading: Guaiacol hydrodeoxygenation study, Appl. Catal. B Environ. 113–114 (2012) 296–307, https://doi.org/10.1016/j.apcatb.2011.11.051.

[93] D.P. Dworak, M.D. Soucek, Synthesis of cycloaliphatic substituted silane monomers and polysiloxanes for photocuring, Macromolecules 37 (2004) 9402–9417, https://doi.org/10.1021/ma048998w.

[94] K. Hayasaka, K. Kamata, H. Nakazawa, Highly efficient olefin hydrosilylation catalyzed by iron complexes with iminobipyridine ligand, Bull. Chem. Soc. Jpn. 89 (2016) 394–404, https://doi.org/10.1246/bcsj.20150359.

[95] A. Gorczyński, M. Zaranek, S. Witomska, A. Bocian, A.R. Stefankiewicz, M. Kubicki, V. Patroniak, P. Pawluć, The cobalt(II) complex of a new tridentate schiff-base ligand as a catalyst for hydrosilylation of olefins, Catal. Commun. 78 (2016) 71–74, https://doi.org/10.1016/j.catcom.2016.02.009.

[96] S. Poonpong, S. Dwivedi, T. Taniike, M. Terano, Structure-performance relationship for dialkyldimethoxysilane as an external donor in stopped-flow propylene polymerization using a ziegler-natta catalyst, Macromol. Chem. Phys. 215 (2014) 1721–1727, https://doi.org/10.1002/macp.201400157.

[97] Q. Zhou, T. Zheng, H. Li, Q. Li, Y. Zhang, L. Zhang, Y. Hu, Effects of some new alkoxysilane external donors on propylene polymerization in MgCl2-supported ziegler-natta catalysis, Ind. Eng. Chem. Res. 53 (2014) 17929–17936, https://doi.org/10.1021/ie5034123.

[98] R. Chakraborty, M.D. Soucek, Synthesis and characterization of cycloaliphatic siloxanes copolymers. ACS Symp. Ser., American Chemical Society, 2010, pp. 27–46, https://doi.org/10.1021/bk-2010-1051.ch004.

[99] E.T. Kopesky, G.H. McKinley, R.E. Cohen, Toughened poly(methyl methacrylate) nanocomposites by incorporating polyhedral oligomeric silsesquioxanes, Polym. (Guildf.) 47 (2006) 299–309, https://doi.org/10.1016/j.polymer.2005.10.143.

[100] T.L. Lu, G.Z. Liang, K.C. Kou, Z.A. Guo, Review synthesis and characterization of cage octa(cyclohexylsilsesquioxane), J. Mater. Sci. 40 (2005) 4721–4726, https://doi.org/10.1007/s10853-005-0839-9.

[101] A. Mabrouk, X. Erdocia, M.G. Alriols, J. Labidi, Economic analysis of a biorefinery process for catechol production from lignin, J. Clean. Prod. 198 (2018) 133–142, https://doi.org/10.1016/j.jclepro.2018.06.294.

[102] M.B. Griffin, K. Iisa, A. Dutta, X. Chen, C.J. Wrasman, C. Mukarakate, M.M. Yung, M.R. Nimlos, L. Tuxworth, X. Baucherel, S.M. Rowland, S.E. Habas, Opening pathways for the conversion of woody biomass into sustainable aviation fuel via catalytic fast pyrolysis and hydrotreating, Green. Chem. 26 (2024) 9768–9781, https://doi.org/10.1039/d4gc03333g.